**Title:** Grasping with a twist: Dissociating action goals from motor actions in human frontoparietal circuits

**Running Title:** Decoding of isolated and task-directed grasping

**Authors:** Guy Rens[1,2,3], Teresa D. Figley[4], Jason P. Gallivan[5], Yuqi Liu[6,7], Jody C. Culham[1,4]

[1]Department of Psychology, University of Western Ontario, London, Ontario, Canada
[2]Laboratorium voor Neuro- en Psychofysiologie, Department of Neurosciences, KU Leuven, Belgium
[3]Leuven Brain Institute, KU Leuven, Belgium
[4]Graduate Program in Neuroscience, University of Western Ontario, London, Ontario, Canada
[5]Departments of Psychology & Biomedical and Molecular Sciences, Centre for Neuroscience Studies, Queen's University, Kingston, Ontario, Canada
[6]Department of Neuroscience, Georgetown University Medical Center, Washington, DC, 20057, USA
[7]Institute of Neuroscience, CAS Center for Excellence in Brain Sciences and Intelligence Technology, Chinese Academy of Sciences, Shanghai, China

***Corresponding Author:**
Guy Rens
The Brain and Mind Institute
University of Western Ontario
Ontario N6A 3K7, Canada
grens@uwo.ca

**Acknowledgements:** This work was supported by grants from the Canadian Institutes of Health Research Operating Grant (MOP84293 to J.C.C.) and Natural Sciences and Engineering Research Council of Canada (to J.C.C.) CIHR-Doctoral Research Award 215131 (T.D.F).

**Conflict of interest:** The authors declare no conflicts of interest.

**Abstract**

In daily life, prehension is typically not the end goal of hand-object interactions but a precursor for manipulation. Nevertheless, functional MRI (fMRI) studies investigating manual manipulation have primarily relied on prehension as the end goal of an action. Here, we used slow event-related fMRI to investigate differences in neural activation patterns between prehension in isolation and prehension for object manipulation. Eighteen participants were instructed either to simply grasp the handle of a rotatable dial (isolated prehension) or to grasp and turn it (prehension for object manipulation). We used representational similarity analysis to investigate whether the experimental conditions could be discriminated from each other based on differences in task-related brain activation patterns. We also used temporal multivoxel pattern analysis to examine the evolution of regional activation patterns over time. Importantly, we were able to differentiate isolated prehension and prehension for manipulation from activation patterns in the early visual cortex, the caudal intraparietal sulcus, and the superior parietal lobule. Our findings indicate that object manipulation extends beyond the putative cortical grasping network (anterior intraparietal sulcus, premotor and motor cortices) to include the superior parietal lobule and early visual cortex.

**Significance statement**

A simple act such as turning an oven dial requires not only that the central nervous system encode the initial state (starting dial orientation) of the object but also the appropriate posture to grasp it in order to achieve the desired end state (final dial orientation) and the motor commands to achieve that state. Using advanced temporal neuroimaging analysis techniques, we reveal how such actions unfold over time and how they differ between object manipulation (turning a dial) vs. grasping alone. We find that a combination of brain areas implicated in visual processing and sensorimotor integration can distinguish between the complex and simple tasks during planning, with neural patterns that approximate those during the actual execution of the action.

## Introduction

The hand is central in physical interactions with our environment. Typical hand-object interactions consist of sequential phases, starting with reaching and ending with object manipulation (Castiello, 2005). Electrophysiological studies in macaques have implicated a frontoparietal network in hand-object interactions (for a review see Gerbella et al., 2017). Previous functional MRI (fMRI) research (for a review see Errante et al., 2021) has identified a similar network in humans. This network comprises a dorsomedial pathway, consisting of the superior parietal occipital cortex (SPOC, corresponding to V6/V6A) and the dorsal premotor cortex (PMd), and a dorsolateral pathway, consisting of anterior intraparietal sulcus (aIPS) and ventral premotor cortex (PMv).

While past human neuroimaging studies revealed the neural substrates of grasping, most treated prehension as the end goal, not as a step towards meaningful hand-object interactions. In contrast, real-world hand-object interactions typically involve grasping only as a prelude to subsequent actions such as manipulating or moving objects. Importantly, previous studies have shown that the final action goal shapes prehension: Initial prehension strategies are affected by the goal in the 'end-state comfort' effect (Rosenbaum et al., 1990) and in actions like tool use (Comalli et al., 2016). Moreover, the end goal affects brain responses during action planning and prehension (Fogassi et al., 2005; Gallivan et al., 2016b).

The purpose of the current study was to investigate how isolated and sequential actions unfold differently on a moment-to-moment basis. The temporal unfolding of brain activation during actions has been largely overlooked (or only studied with EEG, without localizing the specific brain regions involved, e.g., Guo et al., 2019). Most studies that have used multivoxel pattern analysis (MVPA) to investigate hand actions have averaged data within time bins for planning and execution (e.g., Gallivan et al., 2011). Notably, several studies have revealed the temporal unfolding of MVPA grasping representations for sequential timepoints (Ariani et al., 2018a; Gallivan et al., 2013). In addition, one study examined isolated (grasping an object) vs. sequential (grasping to move an object to one of two locations) actions, showing that activation patterns could be discriminated across the grasping network even during action planning (Gallivan et al., 2016).

Here we examined (univariate) activation levels and (multivariate) activation patterns (using representational similarity analysis, RSA (Kriegeskorte, 2008). Moreover, we also used a new methodological approach, temporal MVPA (tMVPA; Ramon et al., 2015; Vizioli et al., 2018) to examine the representation similarities across trials for the same and different points in time, separately for isolated vs. sequential actions.

We measured brain activation using fMRI while participants performed a motor task consisting of either simple grasping of a dial (with two possible initial orientations) or grasping followed by rotation of the dial (clockwise or counterclockwise), as one might turn an oven dial (See Figure 1). Based on earlier findings that brain regions within the grasping network plan the full action sequence, and not just the initial grasp (see Gallivan et al., 201), we expected that during the plan phase, as well as the execute phase, tMVPA would reveal representations of the task (grasp vs. turn). Given that visual orientation (Kamitani & Tong, 2005), surface/object orientation (Rice et al., 2007; Shikata et al., 2001; Valyear et al., 2006) and grip orientation (Monaco et al., 2011) are represented in early visual cortex, the caudal intraparietal sulcus (cIPS), and reach-selective cortex (SPOC), respectively, we predicted that the representation of orientation would be biased to the start orientation early in planning, with a greater emphasis on end orientation as the movement progressed. Our approach with tMVPA allowed us to examine, across different regions, how representations unfolded over time for isolated vs. sequential actions. Specifically, we expected that regions sensitive to the kinematics of executed actions (e.g., M1 and S1) would only show highly similar representations during action execution; whereas, regions involved in more abstract features of action planning (e.g., aIPS for coding object shape) would show similar representations across planning and execution.

## Methods

### Participants

Data from sixteen right-handed volunteers was utilized in the analysis (7 males, 9 females, mean age: 24.4 years). Participants were recruited from Western University (London, Ontario, Canada) and provided informed consent in accordance with procedures approved by the University's Health Sciences Research Ethics Board. Data from an additional two subjects (one male and one female) was collected but excluded due to excessive motion artifacts.

### Setup and apparatus

The experimental setup is illustrated in Figure 1A-B. Participants lay supine in a 3-Tesla MRI scanner with the head and head coil tilted approximately 30° to allow for direct viewing without mirrors of a manipulandum positioned above the participant's hips. The manipulandum consisted of a black rotatable dial (9-cm diameter; Figure 1B) with a yellow rectangular handle (5-cm length x 1-cm width x 2-cm depth). The dial was mounted on a black surface. The black surface was positioned such that the dial was approximately perpendicular to the subject's line of gaze and comfortably within reach of their right

122 arm. Two yellow markers were put on the black surface (Figure 1B) indicating the start and end positions
123 for turning the dial. A grey platform (not shown in Figure 1A) was positioned above the participant's lower
124 torso serving as the home/resting position for the right arm between trials. Participants' upper arms were
125 braced above their torsos and just above their elbows (Figure 1A) to limit movement of the shoulder,
126 which can induce motion artifacts in fMRI signals. As such, participants could only rely on elbow
127 flexion/extension and forearm rotation to perform the experimental task. Considering these constraints,
128 the position and orientation of the dial were adjusted for each participant to optimize participant comfort
129 during task performance and ensure the dial remained fully visible. The position of the yellow markers
130 on the black surface was adjusted for each participant individually so that dial rotation would not exceed
131 80% of the participant's maximum range of motion when turning the dial clockwise or counterclockwise.
132 During the experiment, the dial was illuminated from the front by a bright yellow Light Emitting
133 Diode (LED) attached to flexible plastic stalks (Figure 1A; Loc-Line, Lockwood Products, Lake Oswego, OR).
134 A dim red LED (masked by a 0.1° aperture) was positioned approximately 15° of visual angle above the
135 rotatable dial and just behind it to provide a fixation point for participants (Figure 1A-B). Experimental
136 timing (see below) and lighting were controlled with in-house MATLAB scripts (The MathWorks Inc.,
137 Natick, MA).
138
139 Experiment design and timing
140 *Behavioral task.* This experiment was a 2 (starting orientation: left or right) x 2 (action: grasp or
141 turn) delayed movement paradigm (Figure 1C). For each trial, the dial would appear in one of the two
142 yellow-marked starting positions. The grasp condition consisted of reaching towards the dial and
143 squeezing it between the middle phalanges of the index and middle fingers (trial end position shown in
144 Figure 1A; hand shape during grasp shown in Figure 1B). After grasp completion, participants returned
145 their arm back to the home position. In the turn condition, participants performed the same reach-to-
146 grasp action but would then subsequently rotate the dial clockwise or counterclockwise after they grasped
147 the dial in the left or right start position, respectively (Figure 1C). We decided on the index-middle finger
148 grip instead of a more natural variant of precision grasp as this would ensure the grip would be highly
149 similar in all conditions and limit changes to grip angle to optimize end-state comfort (e.g., putting the
150 right-hand thumb further up when planning to turn clockwise and further down when planning to turn
151 the dial counterclockwise). This avoids contaminating neural activation with low-level sensorimotor
152 confounds such as digit positioning. Participants were instructed to keep the timing of all movements as
153 similar as possible, such that the right hand reached from and returned to the home position at the same

154 time (see next paragraph 'Trial Design'). To isolate the visuomotor planning response from the visual and
155 motor execution responses, we used a slow event-related paradigm with 32-s trials, consisting of three
156 phases: 'Presentation', 'Plan' and 'Execute' (see Figure 1D). We adapted this paradigm from previous fMRI
157 studies that successfully isolated delay-period activity from transient neural responses following the onset
158 of visual stimuli and movement execution (Beurze et al., 2007, 2009; Pertzov et al., 2011). Furthermore,
159 using this paradigm in previous work from our group, we were able to successfully isolate and decode
160 planning-related neural activation prior to action execution (Gallivan et al., 2011; Gallivan, McLean, et al.,
161 2013).

162 *Trial design.* Before each trial, subjects were in complete darkness except for the fixation LED
163 upon which participants were instructed to maintain their gaze. The trial began with a 6-s (3 TRs of 2 s
164 each) Presentation phase in which the illumination LED lit up the rotatable dial. After the Presentation
165 phase, the 12-s (6-TR) Plan phase was initiated with a voice cue (0.5-s duration) saying either 'Grasp' or
166 'Turn' to instruct the upcoming action to the participant. Participants could see the object during the
167 presentation phase, thus perceiving the starting orientation of the yellow handle. However, they were
168 instructed to only begin the action after they received the 'Go' cue. After the Plan phase, a 2-s (1-TR)
169 Execute phase began with a 0.5-s beep (the 'Go' cue' ) cueing participants to initiate and execute the
170 instructed action. Performing the entire action, consisting of reaching and grasping (with or without dial
171 turning), took approximately 2 s. The dial remained illuminated for 2 s after the 'Go' cue allowing visual
172 feedback during action execution. After the 2-s Execution phase, the illumination LED was turned off,
173 cueing participants to let go of the dial and return their hand back to the home position. Participants
174 remained in this position for 12 s (6 TRs) in the dark (i.e., the intertrial interval) to allow the BOLD response
175 to return back to baseline before the next trial would be initiated.

176 *Functional runs.* Within each functional run, each of the four trial types (grasp: left or right – turn:
177 from left to right or right to left) was presented five times in a pseudo-randomized manner for a total of
178 20 trials. Each participant performed eight functional runs, yielding a total of 40 trials/condition (160 trials
179 in total). Each functional run took between 10 and 11 minutes. For each participant, trial orders were
180 counterbalanced across all functional runs so that each trial type was preceded and followed equally often
181 by every trial type (including the same trial type) across the entire experiment. During testing, the
182 experimenter was positioned next to the set-up to ensure that the dial was in the correct position before
183 each trial, and manually adjust it if needed.

184 Participants performed a separate practice session before the actual experiment to familiarize
185 them with the motor task and ensure proper execution. The experimental session took approximately

three hours and consisted of preparation (i.e., informed consent, MRI safety, placing the participant in the scanner and setting up the behavioral task), eight functional runs and one anatomical scan. The anatomical scan was collected between the fourth and fifth functional runs to give participants a break from the task.

MRI acquisition

Imaging was performed using a 3-Tesla Siemens TIM MAGNETOM Trio MRI scanner at the Robarts Research Institute (London, ON, Canada). The T1-weighted anatomical image was collected using an ADNI MPRAGE sequence (time to repetition (TR) = 2300 ms, time to echo (TE) = 2.98 ms, field of view = 192 mm x 240 mm x 256 mm, matrix size = 192 x 240 x 256, flip angle = 9°, 1-mm isotropic voxels). Functional MRI volumes sensitive to the blood oxygenation level-dependent (BOLD) signal were collected using a T2*-weighted single-shot gradient-echo echo-planar imaging (EPI) acquisition sequence (TR = 2000 ms, slice thickness = 3 mm, in-plane resolution = 3 mm x 3 mm, TE = 30 ms , field of view = 240 mm x 240 mm, matrix size = 80 x 80, flip angle = 90°, and acceleration factor (integrated parallel acquisition technologies, iPAT) = 2 with generalized auto-calibrating partially parallel acquisitions (GRAPPA) reconstruction. Each volume comprised 34 contiguous (i.e., with no gap) oblique slices acquired at an approximate 30° caudal tilt with respect to the anterior-to-posterior commissure (ACPC) plane, providing near whole brain coverage. We used a combination of parallel imaging coils to achieve a good signal to noise ratio and to enable direct viewing of the rotatable dial without mirrors or occlusion. Specifically, we placed the posterior half of the 12-channel receive-only head coil (6-channels) beneath the head and tilted it at an angle of approximately 20°. To increase the head tilt to approximately 30°, we put additional foam padding below the head. We then suspended a 4-channel receive-only flex coil over the forehead (Figure 1A).

fMRI anatomical data processing

All fMRI preprocessing was performed in BrainVoyager version 22 (Brain Innovation, Maastricht Netherlands). For the present study, we defined regions of interest (ROIs) in surface space instead of volumetric space as it has been shown that cortical alignment improves group results by reducing individual differences in sulcal locations (Fischl et al., 1999; Frost & Goebel, 2012). As such, we performed surface reconstruction (mesh generation) and cortex-based alignment. Given that we relied on the recommended approach and standard settings of BrainVoyager 22, these steps are explained only in brief.

*Folded mesh generation for each participant*. In volumetric space we performed the following steps. First, we corrected for intensity inhomogeneity. Then, we rotated the anatomical data in ACPC

space, due to the experimental head tilt, and normalized to Montreal Neurological Institute (MNI) space. Next, we excluded the subcortical structures (labelled as white matter) and the cerebellum (removed from anatomical) from mesh generation. We then defined the boundaries between white matter and gray matter and between gray matter and cerebrospinal fluid. Finally, we created a folded mesh (surface representation) of only the left hemisphere after removing topologically incorrect bridges (Kriegeskorte & Goebel, 2001). We decided to only investigate the left hemisphere because the motor task involved the right hand only, which previous work has shown predominantly activates the left (contralateral) hemisphere (Cavina-Pratesi et al., 2010, 2018; Gallivan et al., 2011; Gallivan, McLean, et al., 2013).

*Standardized folded mesh generation for each participant.* Briefly, folded meshes created from anatomical files often result in different numbers of vertices between participants. To facilitate cortex-based alignment between participants, folded meshes were first transformed into high-resolution standardized folded meshes. Each folded mesh was first morphed into a spherical representation by smoothing (thus removing differences between sulci and gyri) and correcting for distortion. The spherical representation of each participant mesh was then mapped to a high-resolution standard sphere to create a high-resolution standardized spherical representation of the participant mesh. The vertex position information of the original participant folded (not spherical) mesh was then used to generate a standardized folded mesh for each participant.

*Cortex-based alignment*. Cortex-based alignment was performed following the approach of Frost & Goebel (2012) and Goebel et al. (2006): We aligned all individual standard meshes to a dynamically generated group average target mesh. Before aligning to the dynamic group average, we performed pre-alignment (i.e., rigid sphere alignment). The actual steps of cortex-based alignment generate a dynamic group average (a surface mesh based on all individual meshes) and sphere-to-sphere mapping files for each participant that enable transporting the functional data from each individual to the dynamic group average. Inverse sphere-to-sphere mapping files were also generated, which allows transporting of data (such as regions of interest) from the dynamic group average back to individual meshes.

<u>fMRI functional data processing</u>

*General preprocessing.* All functional runs were screened for motion and magnet artifacts by examining the movement time courses and motion plots created with the motion correction algorithms. Based on this screening, data from two participants was discarded.

Functional runs were co-registered with the anatomical data using boundary-based registration (Greve & Fischl, 2009). We subsequently performed slice-scan time correction, motion correction and MNI

normalization. Next, we performed linear-trend removal and temporal high-pass filtering (using a cut-off of three sine and cosine cycles on the fast Fourier transform of the time courses).

*Volumetric to surface-based time courses.* Volumetric time courses were first aligned with the respective participant's anatomical scan using boundary-based registration to ensure optimal alignment (Greve & Fischl, 2009). Volumetric time courses were then transformed to the respective participant's standardized folded mesh using depth integration along the vertex normal (sampling from -1 to 3 mm relative to the gray-white matter boundary). Once functional runs were transformed into surface space, they were spatially smoothed. Finally, functional runs in individual standard mesh space, could then be mapped onto the dynamic group average mesh using sphere-to-sphere mapping files that were generated during cortex-based alignment. This approach enabled us to model the averaged brain activation across all participants onto the group mesh and define ROIs based on hotspots of strongest activations in surface space.

Defining regions of interest

To localize our regions of interest on the group mesh, we applied a general linear model (GLM) on our data in surface space. Predictors of interest were created from boxcar functions convolved with the two-gamma haemodynamic response function (HRF). We aligned a boxcar function with the onset of each phase of each trial within each run of each participant, with a height dependent upon the duration of each phase. We used 3 TRs for the presentation phase, 6 TRs for the Plan phase and 1 TR for the Execution phase. The six motion parameters (three translations and three rotations) were added as predictors of no interest. Each incorrect trial was also assigned a unique predictor of no interest. All regression coefficients (beta weights) were defined relative to the baseline activity during the intertrial interval. In addition, time courses were converted to percent signal change before applying the random effects GLM (RFX-GLM).

To specify ROIs for our analyses, we searched for brain areas, on the group level, involved in the experimental task. We contrasted brain activation for all three phases with baseline. This contrast was performed across all conditions to ensure that ROI selection based on local activation patterns was not biased by differences between specific conditions (e.g., grasp versus turn). Specifically, the contrast was: {Presentation [$\text{Grasp}_{\text{left}}$ + $\text{Grasp}_{\text{right}}$ + $\text{Turn}_{\text{left to right}}$ + $\text{Turn}_{\text{right to left}}$] + Plan [$\text{Grasp}_{\text{left}}$ + $\text{Grasp}_{\text{right}}$ + $\text{Turn}_{\text{left to right}}$ + $\text{Turn}_{\text{right to left}}$] + Execute [$\text{Grasp}_{\text{left}}$ + $\text{Grasp}_{\text{right}}$ + $\text{Turn}_{\text{left to right}}$ + $\text{Turn}_{\text{right to left}}$]} > baseline. This contrast enabled us to identify regions that showed visual and/or motor activation associated with the task.

In BrainVoyager, area selection on a surface generates a hexagon surrounding the selected vertex. We decided on an area selection size of 100 (arbitrary units) as this value provided a good balance between inclusion of a sufficient number of vertices/voxels around each hotspot for multivariate analyses and avoiding overlap between ROIs (especially in the parietal lobe).

Regions of interest

Selected regions of interest (Figure 2) were defined in the left hemisphere. Most regions of interest were defined using the contrast above (all conditions > baseline), with two exceptions, as detailed below.

First, the involvement of the cortical grasping network (Gerbella et al., 2017) was investigated by including sensorimotor and visuomotor regions (Ariani et al., 2018; Cavina-Pratesi et al., 2018; Fabbri et al., 2016; Gallivan et al., 2011; Gallivan, McLean, et al., 2013).

- Primary motor cortex (M1): Hotspot of strongest activation near the 'hand knob' landmark (Gallivan et al., 2013; Yousry et al., 1997).
- Dorsal premotor cortex (PMd): Hotspot of strongest activation near the junction of the precentral sulcus and the superior frontal sulcus (Picard & Strick, 2001; Pilacinski et al., 2018).
- Ventral premotor cortex (PMv): Hotspot of strongest activation inferior and posterior to the junction of the inferior frontal sulcus) (Tomassini et al., 2007).
- Primary somatosensory cortex (S1): Hotspot of strongest activation anterior to the anterior intraparietal sulcus, encompassing the postcentral gyrus and sulcus (Gallivan et al., 2011; Gallivan, McLean, et al., 2013)
- Anterior intraparietal sulcus (aIPS): Hotspot of strongest activation directly at the junction of the intraparietal sulcus and the postcentral sulcus (Culham et al., 2003).
- Caudal intraparietal sulcus (cIPS): Hotspot of strongest activation on the lateral side of the brain, anterior and superior to the junction between the intraparietal sulcus and the posterior occipital sulcus (Beurze et al., 2009; Grefkes & Fink, 2005). Comparisons with the Julich atlas (Richter et al., 2019) suggested overlap with hIP7 and/or hP01.
- Anterior superior parietal occipital sulcus (aSPOC): Hotspot of strongest activation on the medial side of the brain, anterior and superior to the parietal-occipital sulcus (Cavina-Pratesi et al., 2010), thought to correspond to area V6A (Pitzalis et al., 2015).
- Posterior superior parietal occipital sulcus (pSPOC): Hotspot of strongest activation on the medial side of the brain, posterior and inferior to the parietal-occipital sulcus (Cavina-Pratesi et al., 2010). thought to correspond to area V6 (Pitzalis et al., 2015).

313 Second, the following medial and frontal regions were selected due to their involvement in motor
314 planning and decision making (Ariani et al., 2015; Badre & Nee, 2018; Cavina-Pratesi et al., 2018).

315 - Dorsolateral prefrontal cortex (DLPFC): Hotspot of strongest activation near the middle
316 frontal gyrus (Mylius et al., 2013).
317 - Supplementary motor area (SMA): hotspot of strongest activation adjacent to the medial end
318 of the cingulate sulcus and posterior to the plane of the anterior commissure (Picard & Strick,
319 2001).
320 - Pre-supplementary motor area (pre-SMA): Hotspot of strongest activation superior to the
321 cingulate sulcus, anterior to the plane of the anterior commissure and anterior and inferior
322 to the hotspot of strongest activation selected for SMA (Picard & Strick, 2001).

323 Third, we included the superior parietal lobule (SPL) due to the extensive activation evoked by our task
324 and in hand actions more generally (Ariani et al., 2018a; Cavina-Pratesi et al., 2018). We defined the SPL
325 as the area on the lateral/superior side of the brain that is bordered anteriorly by the postcentral sulcus,
326 inferiorly by the intraparietal sulcus and posteriorly by the parietal-occipital sulcus (Scheperjans, et al.,
327 2008a; Scheperjans et al., 2008b). Due to the large swathe of activation evoked by our contrast, we
328 defined four ROIs within the SPL based on their relative position to each other (to ensure minimal overlap)
329 and the anatomical landmarks bordering the SPL. We decided on four ROIs as well as their names based
330 on Scheperjans et al. (2008a).

331 - 7PC: Hotspot of strongest activation located on the posterior wall of the postcentral sulcus and
332 superior to the intraparietal sulcus. Given we defined post-aIPS as well, 7PC was also defined as
333 superior to post-AIPS.
334 - 5L: Hotspot of strongest activation located just posterior to the postcentral sulcus and superior to
335 area 7PC.
336 - 7P: Hotspot of strongest activation superior to the intraparietal sulcus and anterior to the parietal-
337 occipital sulcus.
338 - 7A: Hotspot of strongest activation in the postcentral gyrus, superior to 7PC, posterior to 5L and
339 anterior to 7P.

340 Finally, two visual regions were selected from a probabilistic functional atlas that utilized cortex-based
341 alignment (Rosenke et al., 2021), to which we aligned our participant surface meshes.

342 - Dorsal primary visual cortex (V1d): Given that primary visual cortex (V1) responds to visual
343 orientation (Kamitani & Tong, 2005a) we wanted to investigate its response here. Because our
344 target objects (and participants hands) fell within the lower visual field (below the fixation point),

345 they would stimulate the dorsal divisions of early visual areas (Wandell et al., 2007). As such, we
346 investigated only the dorsal division of V1, V1d, using the Rosenke atlas.
347 • Extrastriate body area (EBA): We were also interested in examining the response of the
348 extrastriate body area, which has been implicated not only in the visual perception of bodies
349 (Greenfield et al., 1996) but also in computing goals during action planning (Astafiev et al., 2004;
350 Zimmermann et al., 2016). Because the EBA is not easy to distinguish from nearby regions of the
351 lateral occipitotemporal cortex, we utilized the EBA from the Rosenke atlas.
352 After ROIs were defined in group surface space, they were transformed to individual surface space, using
353 the inverse transformation files generated during cortex-based alignment and then to individual
354 volumetric MNI space, using depth expansion (inverse of depth integration; see 'fMRI functional data
355 processing: Volumetric to surface-based time courses') along the vertex normals (-1 to 3 mm). This
356 approach allowed us to define ROIs on the group surface but extract functional data from the individual
357 volumetric level.
358
359 Analysis of functional data
360 Functional data were extracted to perform deconvolution general linear models (deconvolution GLMs;
361 (Hinrichs et al., 2000), representational similarity analysis (Kriegeskorte, 2008) and temporal multivoxel
362 pattern analysis (tMVPA; (Vizioli et al., 2018). All analyses described below, excluding initial processing of
363 fMRI data and the univariate analyses (which where both done in BrainVoyager), were done with in-house
364 MATLAB scripts.
365 *Univariate analysis.* We used a random-effects GLM with deconvolution to extract the time
366 courses of activation in each ROI during the experimental task. For each experimental condition, we used
367 15 matchstick predictors, the first of which was aligned with time point zero (Figure 1D; "light on"). For
368 each functional voxel in each ROI, baseline *z*-normalized estimates of the deconvoluted BOLD response,
369 representing the mean-centered signal for each voxel and condition relative to the standard deviation of
370 signal fluctuations, were extracted for all conditions. Voxel activation was then averaged across voxels
371 within each ROI. This provided us with an estimate of the averaged time course of brain activation for
372 each condition for each ROI and for each participant.
373 *Temporal multivoxel pattern analysis.* For tMVPA we relied on the approach developed in Ramon
374 et al. (2015) and Vizioli et al. (2018). Briefly, tMVPA has been developed to investigate the temporal
375 development of neural representations by relying on multivariate analyses with a trial wise approach. The
376 tMVPA methods are schematized in Figure 3. For each voxel of each ROI of each participant, we performed

377 a deconvolution GLM for every trial separately, which was then transformed into BOLD percent signal
378 change by dividing the raw BOLD time course by its mean. Note that for tMVPA we performed
379 deconvolution GLMs for each trial (of the same condition) separately whereas for the univariate analysis
380 and RSA (see below) we ran deconvolution GLMs for each condition (i.e., across same-condition trials).
381 After computing the single-trial activation patterns, we computed single-trial representational
382 dissimilarity matrices (stRDMs; dissimilarity = 1 - *r*) using Pearson correlation for each condition of each
383 ROI of each participant. As shown in Figure 3A, a stRDM is generated by computing dissimilarity between
384 the activation patterns of voxels at each timepoint of a given trial ('trial m') with the activation pattern of
385 the same voxels for each of the timepoints for another trial ('trial n'). This process is iteratively repeated
386 until all unique within-condition trial pairings are run. stRDMs were then averaged across the main
387 diagonal to yield a diagonally symmetric matrix. We performed this averaging as we were only interested
388 in between-condition differences and not in differences between same-condition trials.

389 To further clarify calculation of the dissimilarity metric: in Figure 3B and Figure 3C, the green
390 highlighted square indicates the dissimilarity between all the voxels (of a given ROI) at timepoint 2 of Turn
391 Left to Right trial m with the activation of the same voxels at timepoint 2 of Turn Left to Right trial n. The
392 magenta highlighted squares indicate the averaged dissimilarity between timepoints 2 and 10 of trial m
393 and n. As explained before, we averaged the dissimilarity between timepoint 2 of trial m and timepoint
394 10 of trial n (magenta highlighted square below diagonal) with the dissimilarity between timepoint 10 of
395 trial m and timepoint 2 of trial n (magenta highlighted square above diagonal). Finally, the blue highlighted
396 square indicates the dissimilarity between timepoints 10 of trial m and n. In sum, values on the main
397 diagonal show dissimilarity between within-condition trials at the same timepoint. Values that are off the
398 main diagonal show the dissimilarity between within-condition trials at different (i.e., earlier or later)
399 timepoints.

400 stRDMs were calculated for the four conditions separately, Fisher *z*-transformed and then
401 averaged (10 % trimmed mean; Vizioli et al., 2018) within conditions (e.g., average RDM for grasp left).
402 Finally, the averaged RDMs were then averaged across orientations (e.g., averaging of RDMs between left
403 and right start orientations to produce average Grasp and Turn RDMs; Figure 3D and 3E respectively). This
404 was done as we were primarily interested in investigating differences in neural representations between
405 singular (grasping) and sequential actions (grasping then turning) and we did not expect that these
406 differences would depend upon the start orientation. As such, this approach resulted in two RDMs for
407 each participant.

408 In line with Vizioli et al. (2018), we performed statistical analysis on the Fisher *z*-transformed data;
409 however, we used the non-transformed data for visualization purposes to render the values visually more
410 interpretable. To test for statistically significant differences between the grasp and turn RDMs, we
411 subtracted for each participant the turn RDM from the grasp RDM resulting in a subtraction matrix (Turn
412 versus Grasp: Figure 3F) and investigated where the subtraction differed significantly from zero. As such,
413 a given value in the subtraction matrix that is positive indicates that grasping trials are more dissimilar
414 than turning trials at that given timepoint. Conversely, a value that is negative indicates that turning trials
415 are more dissimilar than grasping trials at that given timepoint. Note that we decided to statistically test
416 whether each cell differed from zero instead of the increasingly larger sliding window analysis used in
417 Ramon et al. (2015) and Vizioli et al. (2018). Our rationale was that the earlier studies relied on a visual
418 task (face recognition) whereas our study relied on a motor task. Arguably, during motor
419 preparation/execution, neural representations might evolve differently than purely visual responses. As
420 such, we argued that statistically testing each cell separately might reveal more information on the
421 temporal evolution of motor execution as, for instance, transitions between activation patterns between
422 planning and execution might be brief or abrupt. Note that because we had averaged values across the
423 main diagonal when calculating the dissimilarity matrices (Figure 3 and 5), these matrices were
424 symmetrical reflections across the diagonal. However, we performed statistical analyses only on the
425 values on and above the main diagonal of the Turn versus Grasp subtraction matrices (Figure 3F). To test
426 for statistical significance, we performed (1 - alpha) bootstrap confidence-interval analysis by sampling
427 participants with replacement 500 times. Within each ROI, we accounted for multiple comparisons using
428 Bonferroni correction. Importantly, we decided to exclude the first two timepoints (TRs) and the last one
429 from the statistical analyses because no differences were expected before the BOLD response to emerge
430 at the start, because later timepoints reflect the post-stimulus undershoot phase of the BOLD response,
431 and to reduce the number of comparisons requiring Bonferroni correction for multiple comparisons.
432 *Hierarchical clustering.* The tMVPA matrices (stRDMs) for Grasp and Turn revealed that different
433 ROIs showed different temporal unfolding. For example, some regions showed similar activation patterns
434 throughout the entire trial; whereas, other regions showed similar patterns only during motor execution
435 (See Figure 5). To make it easier to group these different ROI timing patterns for display and discussion,
436 we used hierarchical clustering. To do so, we averaged within-participants the grasp and turn RDMs to
437 generate one RDM per participant. Next, we calculated for each participant the Spearman correlations
438 between all ROIs using the averaged RDMs. The ROI correlation matrix for each participant was then

transformed into a dissimilarity measure (1-*r*). Finally, hierarchical clustering was then performed using the ROI dissimilarity matrix of all participants.

*Representational similarity analysis.* We used RSA to examine the degree to which the pattern of activation across voxels within each ROI at each time point represented the start orientation, the end (goal) orientation, and the task, as illustrated in Figure 4A-C. For RSA, we relied on the methods described in Kriegeskorte (2008). By examining the degree to which different conditions evoke a similar pattern of brain activation within a ROI, the nature of neural coding (or representational geometry; Kriegeskorte & Kievit, 2013) can be assessed. First, we utilized the deconvolution analysis without averaging across voxels within ROIs. For each voxel, the average activation was normalized to a mean of zero by subtracting the mean across conditions from the value of each condition in that voxel (Haxby et al., 2001). This was done for each run separately. This resulted in average temporal development of brain activation for each condition for each voxel of each ROI and for each run of each participant. Then, we computed representational dissimilarity matrices (RDMs) for each timepoint for each ROI of each participant. By computing a Pearson correlation of voxel activation patterns for each timepoint within each ROI (dissimilarity = 1 - *r*), the RDMs can quantify the dissimilarity in activation patterns of one condition with different conditions. To test within-subject reliability of the RDM calculations, we used cross-validation by splitting data into all potential combinations. Split data provides data-based estimates of dissimilarity even for the same condition (e.g., Grasp left in one data split vs. Grasp left in another data split); whereas, in unsplit data, the dissimilarity is necessarily zero. Data for all cells in the RDM is necessary for RSA on factorial designs to ensure that contrasts are balanced across orthogonal factors. Pearson correlations (*r*) were computed between the activation patterns across voxels in each condition during odd and even runs and then Fisher transformed to have a similarity metric with a Gaussian distribution.

To test whether each region contained information about condition differences, we measured correlations between the RDM in each region (Figure 4D-E) and three separate models that capture orthogonal components of the experimental task (Figure 4A-C). This was done for each timepoint separately (15 matchstick predictors; time-resolved decoding). We used three models that capture specific task attributes: (A) Start orientation, irrespective of task (i.e., grasp or turning) — a timepoint with an RDM that correlates with this model would indicate an encoding of the initial orientation of the handle (i.e., left, or right), (B) end orientation, irrespective of the performed action (i.e., grasp or turning) — a timepoint with an RDM that correlates with this model would indicate an encoding of the final orientation of the handle (i.e., left, or right) after task execution, (C) motor task, irrespective of the initial/final handle's orientation (i.e., left, or right) — a timepoint with an RDM that correlates with this model would

indicate an encoding of the task goal  task (i.e., grasping or turning). The metric was calculated by computing the Spearman correlation (ρ) between the Fisher-transformed split RDMs and each model for each ROI for each participant. We used one-way Student's *t* tests to assess whether model correlations were significantly greater than zero and performed corrections for multiple comparisons using the false discovery rate. Corrections for multiple corrections were done for each ROI separately (i.e., 15 timepoints for three models compared to zero for 45 comparisons in total). For each ROI we also calculated the upper and lower bound of the noise ceiling. Briefly, the noise ceiling is the expected RDM correlation achieved by the (unknown) true model, given the noise of the data and provides an estimate of the maximum correlations that could be expected for a given model in a given ROI (Kriegeskorte, 2008). RDMs were first rank transformed, following the original *z*-transformation. The upper bound of the noise ceiling, considered an overestimate of the maximum correlation, was calculated as iteratively correlating one participant's RDM with the average RDM of all participants (thus including the given participant) and then averaging across all participants. The lower bound of the noise ceiling, considered an underestimate of the maximum correlation, was calculated as iteratively correlating between one participant's RDM with the average RDM of all other participants (thus excluding the given participant), and then averaging across participants.

**Results**

Qualitative examination of the deconvolution time courses (Figure 2) and the tMVPA results indicated that different regions had different temporal profiles of activity. As shown in Figure 5, hierarchical clustering of the RDMs averaged across Grasp and Turn facilitated conceptual grouping of the ROIs for further investigation.

Notably, ROIs differed in the time ranges over which they showed reliable activation patterns across trials of the same type. Most strikingly, V1d and cIPS showed strong temporal similarity in activity patterns throughout the Plan and Execute phases of the trial, as indicated by the large block of high similarity (dark red) beginning early in planning and continuing through late execution. That is, in these regions, voxel activation patterns were not only similar during the same phase (along the diagonal cells) but were also similar across timepoints throughout planning and execution (off-diagonal cells in the planning and execution phases). This indicates consistency in the neural representation throughout the trials. Similar but weaker similarity patterns were also observed in other regions, particularly aSPOC, pSPOC, 7P, EBA, 7A , 7PC, and 5L.

502 In contrast, other regions -- aIPS, M1, S1, pre-SMA, SMA, PMd -- showed trial-consistent
503 activation patterns predominantly for the peak execution period (dark red blocks in the execution phase;
504 i.e., in lower right corners of Grasp and Turn matrices). In some cases, there was also some consistency
505 of patterns between the peak execution phase and earlier timepoints during Plan and Execute of which
506 M1 is a clear example in Figure 5 (off-diagonal cells between planning and execution phase, as indicated
507 by the reddish "wings" above and left of the peak similarity). PMv and DLPFC showed only weak
508 consistency of patterns across trials, highest in the peak of execution.
509 Interesting patterns were also observed in the tMVPA difference in trial-by-trial consistency
510 between turn and grasp (final column of Figure 5). Notably many of the regions showed higher
511 consistency during Turn actions than Grasp actions.
512 Based on these observations from Figure 5, we focussed subsequent analysis and interpretation
513 on a subset of ROIs in Figure 6.
514
515 Visual regions of V1d and cIPS
516 *Qualitative assessment of the univariate analysis.* The first column in Figure 6 shows the
517 deconvolution time courses for V1d and cIPS. V1d and cIPS show a steep increase in average voxel
518 activation following object presentation (timepoint 0). This initial increase is followed by a second smaller
519 increase halfway through the planning phase and, last, by a third and final increase following action
520 execution. Although V1d and cIPS are primarily visual regions, the univariate analysis shows that activation
521 does not remain constant throughout the visual presentation of the stimuli, but is modulated by the
522 dynamics of the task.
523 *Qualitative assessment of the condition RDMs.* In Figure 6 the second and third columns show the
524 condition RDMs for grasp and turn, respectively. For both regions, activation pattern similarity within
525 conditions strongly increases following object presentation. Due to the sluggish nature of the
526 hemodynamic response and our findings for the univariate analysis, it is plausible that this early increase
527 of similarity in the activation patterns is primarily driven by a visual response. Notably, the cIPS within-
528 condition similarity in activation patterns increases towards the peak execution (approx. timepoint 11-
529 13).
530 *Temporal multivoxel pattern analysis*. The fourth column in Figure 6 depicts the subtraction Turn
531 minus grasp on which we performed statistical analyses as previously described. For V1d, tMVPA is unable
532 to discriminate the grasp and turning condition for matched timepoints (along the diagonal) during motor
533 planning. That is, subtracting the grasp dissimilarity from the turn dissimilarity (second and third column

534 in Figure 6) does not result in a difference that differs statistically from zero. Interestingly, tMVPA is able
535 to discriminate the activation patterns of grasping and turning during late execution (i.e., the "plus sign"
536 significant squares in the grasp versus turn RDM for V1d). In addition, tMVPA was also able to discriminate
537 activity patterns related to grasping versus turning when dissimilarity calculations were done between
538 timepoints of the late planning phase and timepoints of the late execution phase (i.e., the three adjacent
539 significant squares in the grasp versus turn RDM for V1d). These findings suggest that the activation
540 patterns in V1d become tuned towards either grasping or turning during late motor planning. Similar but
541 stronger effects were found for cIPS. tMVPA was able to discriminate cIPS activation patterns during most
542 of the execution phase as well as when dissimilarity calculations were done between timepoints of the
543 execution phase and early and late timepoints of the planning phase (i.e., the vertical and horizontal
544 "wings" of significant squares above and left of the execution phase). This suggests that in cIPS,
545 representations of the task emerge early in the planning period.

546 *Representational similarity analysis.* For the RSA, we tested how well multivariate activation
547 patterns fit three models for the representation of start orientation, end orientation, and task (Turn versus
548 Grasp) over time (Figure 6; last column). Notably, although all three types of information appear to be
549 represented in both V1d and cIPS during action execution, only starting orientation appeared to be
550 represented during the planning phase (Figure 6; last column; V1d and cIPS; green trace). Although the
551 decoding of start orientation during planning and end orientation during execution may reflect the
552 processing of simple visual orientation information (Kamitani & Tong, 2005), coding of both start and end
553 orientation overlapped during execution (Figure 6; last column; V1d and cIPS; green and red trace),
554 suggest a much more complex representation. Notably, V1d, represented the task during late planning,
555 before any action had been initiated, perhaps due to anticipation of the visual consequences of the
556 upcoming action.

557 In sum, while our findings are consistent with a role for V1d and cIPS as predominantly visual
558 regions, the two multivariate analyses (tMVPA and RSA) suggested that these regions discriminate
559 between grasping and turning actions not only during action execution but also during motor planning.

560

561 <u>Regions of the SPL: 7A, 7PC, 5L and 7P</u>

562 *Qualitative assessment of the univariate analysis.* As shown in the first column in Figure 6, our
563 results suggest multiple ROIs within the SPL have a visuomotor involvement in hand-object interactions.
564 All four regions show three distinct peaks, two of comparable amplitude following the onset of visual
565 stimulation and the planning instruction, with a larger peak during action execution. This change in

566 average activation is more distinctly visible for regions 7A and 5L as their activation peaks higher during
567 the execution phase compared to the regions 7PC and 7P.

568 *Qualitative assessment of the condition RDMs.* The condition RDMs of Figure 6 show that the ROIs
569 within the SPL show activity patterns that are similar to each other. First, similarity between trials within
570 each condition increases following object presentation, in particular, during early planning. Second,
571 similarity in activation patterns is then maintained until a second increase during the execution phase.
572 Notably, this pattern (in the condition RDMs of the SPL regions) is similar to that of V1d and cIPS, albeit
573 much weaker. Most importantly, the increase in within-condition trial similarity following object
574 presentation is much weaker for the SPL regions than for V1d and cIPS. This suggests that these regions
575 encode visual information to a lesser extent than V1d and cIPS and might be more involved in visuomotor
576 transformation of visual cues into executable motor commands.

577 *Temporal multivoxel pattern analysis*. In line with the qualitative assessments of the univariate
578 analysis and the condition RDMs, tMVPA suggests a role for the regions of the SPL throughout the trial,
579 but particularly during motor execution (Figure 6; column 4). For 7A, tMVPA was able to discriminate
580 activation patterns for grasping and turning during the later execution phase. Interestingly, we found
581 similar results for 7PC as for cIPS (as explained in "Visual regions of V1d and cIPS"). tMVPA was able to
582 discriminate grasping and turning throughout both earlier and later stages of the execution phase as well
583 as when dissimilarity calculations were done between timepoints of the planning phase and timepoints
584 of the execution phase. These findings indicate that 7PC might anticipate turning actions already during
585 the planning phase. The results for 5L are somewhat similar to the findings for 7A and 7PC. That is, tMVPA
586 is able to differentiate between grasping and turning during the later execution phase but also when
587 dissimilarity was calculated on timepoints of the early/late planning phase and timepoints of the
588 execution phase. For 7P, tMVPA could significantly discriminate activation patterns associated with
589 grasping and turning only during the execution phase. Finally, it can be seen that tMVPA can discriminate
590 between grasping and turning by relying on the activation patterns of each of the four regions. However,
591 this ability to discriminate the task is the weakest in 7PC, stronger in 7A and 5L and the strongest in 7PC.

592 *Representational similarity analysis.* The RSA results (Figure 6 column 5) further support that the
593 regions of the SPL are rather visuomotor than purely visual: starting orientation cannot be decoded from
594 the SPL (Figure 6; last column; 7P, 7A, 7PC and 5L; green trace) during the planning phase as for V1d and
595 cIPS. In support of our tMVPA results, grasping versus turning can be decoded from all four regions in the
596 SPL (Figure 6; last column; 7P, 7A, 7PC and 5L; blue trace). RSA is primarily able to do this when relying on
597 the execution phase significant decoding is also observed during the late planning phase for the regions

598 7A and 7P. Interestingly, in 7PC only turning versus grasping can be decoded, suggesting that this region
599 might be mainly involved in rotating the wrist, irrespective of the direction. Indeed, from the other regions
600 (7A, 5L and 7P) both start and end orientation can be decoded during the action execution phase
601 suggesting that these regions encode specific wrist orientations throughout the hand-object interaction.
602 In sum, our multivariate analyses provide evidence for the involvement of the SPL in decoding
603 sequential actions. That is, sequential (grasping then turning) actions can be differentiated from singular
604 grasping actions based on the activation patterns from the regions 7A, 7PC, 5L and 7P, in some cases even
605 before action execution.
606
607 EBA and aIPS
608 *Qualitative assessment of the univariate analysis.* As shown in Figure 6, aIPS shows a modest visual
609 response, with a distinct "bump" in the planning phase and following execution, indicating involvement
610 in both motor planning and execution. EBA shows an initial visual response following object presentation
611 after which activation wanes until action execution. However, following action execution, activation
612 increases again suggesting an involvement of EBA in action execution, perhaps related to the visualization
613 of the arm and hand with respect to the object.
614 *Qualitative assessment of the condition RDMs.* In line with the univariate analysis, the condition
615 RDMs for aIPS show that similarity in activation patterns remains very low until motor action and then
616 sharply increases following action execution. As such, the condition RDMs indicate that aIPS is primarily
617 involved in action execution. In the condition RDMs for EBA, a clear visual response can be seen as within-
618 condition similarity increases early during trials. Interestingly, in line with the univariate analysis, within-
619 condition similarity increases again following task execution further supporting the notion of EBA's
620 involvement in motor execution and/or visual feedback of the hand.
621 *Temporal multivoxel pattern analysis*. tMVPA can discriminate activation patterns in aIPS related
622 to grasping and turning during the early execution phase, again supporting the notion that aIPS is involved
623 in the execution of hand-object interactions. Interestingly, tMVPA was able to discriminate activation
624 patterns related to grasping and turning during the planning phase as well as when dissimilarity was
625 calculated between timepoints of the planning phase and timepoints of the execution phase. EBA showed
626 sporadically significant differences between the two tasks during the early visual response and planning.
627 *Representational similarity analysis.* From aIPS, RSA could discriminate the activation patterns
628 associated with grasping and turning during the planning phase as well as during the execution phase
629 (Figure 6; last column; aIPS; blue trace). For EBA, the RSA revealed an early visual response as it was able

630 to decode starting orientation from the activation patterns following object presentation (Figure 6; last
631 column; EBA; green trace). Interestingly, in with the previous analyses, RSA was able to decode grasp
632 versus turn in both the planning phase as well as the execution phase (Figure 6; last column; EBA; blue
633 trace).

634 In sum, our findings for aIPS are in line with previous studies that showed its involvement in motor
635 planning and execution (e.g., Singhal et al., 2013). Interestingly, our multivariate analyses support the
636 suggestion that EBA, perhaps along with hand-selective divisions of the lateral occipitotemporal cortex, is
637 not a purely visual region but is also involved in analyzing visual feedback of the body and hand during
638 motor execution (Astafiev et al., 2004; van den Heiligenberg et al., 2018; Zimmermann et al., 2016)

639

640 Other regions of interest

641 We focussed the presentation of the results above in the most robust and interesting findings
642 about how hand-object interactions unfold over time. Other regions showed effects that were weaker or
643 less surprising. The condition RDMs and tMVPA results for the previously discussed ROIs and other ROIs
644 can be found in Figure 6. Full results figures for all ROIs can be found on GitHub
645 (https://github.com/GuyRens/OvenDials).

646 Briefly, we found no robust effects for the parietal regions of pSPOC and aSPOC which have been
647 considered to be typically involved in hand-object interactions. A similar absence was found for the DLPFC
648 and for the secondary motor regions PMv, SMA and pre-SMA. However, tMVPA was able to discriminate
649 activation patterns related to grasping and turning during the execution phase from both PMd and S1
650 which is in line with previous work suggesting their involvement in the execution of hand-object
651 interactions. Finally, for PMd and S1, tMVPA was able to discriminate grasping and turning activation
652 patterns during the early execution phase.

653

654 **Discussion**

655 Our results (summarized by the outlined circles in Figure 2) provide new insights into how neural
656 representations over time for a simple prehension task vs. a more complex manipulation task. While prior
657 work has shown that different types of grasp sequences can be decoded (Gallivan et al., 2016), the current
658 study examines the temporal coding of this information across planning and execution, as well as the
659 nature of the information being represented in individual brain regions over time. In addition, our study
660 examines the activity of regions within the SPL, not previously explored in the prior work. Our additions

661 corroborate earlier findings (Gallivan et al., 2016, 2019) that action sequences are represented in visual
662 areas (such as V1 and EBA), but also implicate subdivisions of the SPL (areas 7A, 7PC, 7P and 5L).
663 Using RSA, we found that while some regions, particularly V1, coded start orientation during
664 planning, multiple regions (V1, cIPS, SPL and EBA) coded a combination of start orientation, end
665 orientation and task during execution. This finding suggests that the activation patterns in these areas
666 reflect more than simple visual-perceptual information such, as the visual orientation of the dial (Kamitani
667 & Tong, 2005); instead, these patterns reflect the combination of the initial goal, the motor specific act,
668 and the final outcome. Moreover, the similarity of activation patterns across planning and execution, as
669 identified through our tMVPA, suggests that an action and its outcome are anticipated well before the
670 movement begins.
671
672 Temporal Unfolding of Complex vs. Simple Actions
673 We investigated the temporal unfolding of complex vs. simple actions using multiple measures of
674 neural responses: univariate time courses (Figure 1), RSA for sequential volumes (Figures 4 and 6) and,
675 tMVPA (Figures 3, 5 and 6). These different measures provide a fuller picture of how actions unfold over
676 time than considering each approach in isolation. For example, univariate signals reveal that both V1 and
677 cIPS show robust visual signals in all three phases of the trial (presentation, plan and execute), as do SPL
678 regions and EBA to a lesser degree. tMVPA shows consistency in the patterns of activation in these areas
679 throughout the trial. However, RSA shows that different areas are representing different kinds of
680 information at different points in the trial. For example, V1 represents start orientation early in the trial
681 and task later, while 7P represents both pieces of information only just before execution begins.
682 Moreover, tMVPA shows that trial similarity remains high in all these regions through both Grasp and Turn
683 trials, but trial-by-trial similarity during execution and between execution and planning is higher for Turn
684 than Grasp trials.
685 These results build upon earlier work examining univariate and multivariate time courses during
686 grasping (Ariani et al., 2018b; Gallivan et al., 2016a). They also provide a valuable complement for EEG
687 studies that reveal temporal coding with even finer temporal resolution but poorer spatial resolution. An
688 EEG study by (Guo et al., 2019) showed that grasp orientation (defined by instruction rather than object
689 attributes) can be classified during both a visual preview and action execution, with similar
690 representations between the two phases; moreover, their most informative electrodes were over left
691 caudal parietal cortex, though source localization indicated diverse potential sources (that may include
692 cIPS, SPL, and EBA).

One of the more surprising results of the current study was the strong involvement of SPL in showing differences between Turn and Grasp actions. The role of the SPL in hand actions has been relatively less studied than areas in the IPS (especially cIPS and aIPS) and SPOC (V6/V6A), for which clear homologies between humans and other primates have been proposed (Culham & Kanwisher, 2001; Grefkes & Fink, 2005). One partial exception is area 7PC, an SPL region dorsal to aIPS, that has been proposed as the human homologue of the macaque medial intraparietal sulcus (mIPS) and/or parietal reach region (PRR), albeit with limited consensus about locus (Gallivan & Culham, 2015) and putative homologies (Culham et al., 2006). These SPL areas likely form part of the dorsomedial (or dorsal-dorsal) visual stream (Rizzolatti & Matelli, 2003) and have been postulated as an integration zone for visual, motor, and somatosensory information for goal-directed movements (Passarelli et al., 2021). Human and macaque SPL have similar structural organization with the anterior sector -- 7PC (macaque homologue: VIP; Caminiti et al., 2015) and 5L (macaque homologue: PE; Gamberini et al., 2020) -- being predominantly somatosensory and the more caudal parts -- 7A (macaque homologue: PEc; Gamberini et al., 2020) and 7P (macaque homologue: V6A; Gamberini et al., 2020) -- being both somatosensory and visual (Gamberini et al., 2020). The anterior regions of the SPL (5L and 7PC) fall on the more somatosensory side of the visual-to-somatosensory gradient from the posterior to anterior SPL. As such, they may be involved in anticipating the sensory (perhaps largely somatosensory) and motor requirements and consequences of the action.

<u>Orientation Processing</u>

Our experiment explicitly involved tasks that required processing of object orientation for grasping and turning. While processing of object location for reaching and object shape and size for grasping have been well characterized behaviorally and neurally (Cavina-Pratesi et al., 2010), the influence of object orientation on reach-to-grasp actions has only recently been investigated in the monkey and human. These studies have suggested that object orientation and/or wrist/grip orientation rely on V6A/aSPOC (Battaglini et al., 2002; Monaco et al., 2011) and the adjacent cIPS (Rice et al., 2007; Shikata et al., 2001; Valyear et al., 2006) perhaps along with aIPS (Breveglieri et al., 2022). One fMRI study that had participants grasp a dial much like ours found that “bistable” object orientations (which equally afforded two possible grip postures) evoked greater activation in cIPS than stable orientations (which afforded only one grip posture) (Wood et al., 2017). Moreover, this study found that two neuropsychological patients with unilateral damage to cIPS showed deficits in grasping bistable orientations with the contralateral hand. We find that cIPS codes a combination of start orientation, end

725 orientation, and task during action execution. Moreover, cIPS activation is more consistent throughout a
726 trial in a complex turning task, where object orientation must be changed through a grip rotation, than a
727 simpler grasp-only task, corroborating the proposed role of cIPS in processing orientation for action. To
728 our surprise, we did not observe any orientation coding in aSPOC or pSPOC.

729 Akin to cIPS, early visual cortex has been increasingly implicated in motor planning and execution
730 (Gallivan et al., 2014, 2019; Gutteling et al., 2015; Monaco et al., 2020). We show that the visual cortex
731 (V1) codes the start orientation of the object throughout the trial with increases in the task representation
732 toward the end of planning and during execution. This suggests that V1 activation patterns are not solely
733 driven in a bottom-up fashion by current visual cues (Kamitani & Tong, 2005) but come to incorporate the
734 complexity of the task and visual information as the action unfolds.

735 Although studies of EBA have focused on its role in body perception (Kontaris et al., 2009), EBA
736 has also been implicated in processing body posture during planning and execution of goal-directed
737 actions (Gallivan et al., 2016; Zimmermann et al., 2018). We found some evidence for this notion: EBA has
738 strong representations of task and orientations during execution but only limited ones during planning.
739 As such, EBA may be mainly driven by the perceptual consequences of the action.

740

741 Methodological considerations

742 Our "grasping" actions were atypical in that they required gripping the dial between the
743 knuckles of the index and middle fingers, in a way that was similar between grasping, turning to the left,
744 and turning to the right. This choice of posture was deliberate, to ensure that the representations of the
745 upcoming task were not confounded with differences in initial grip posture. Nevertheless, this strategy
746 differs considerably from the approach that participants would likely have undertaken without such
747 instruction. That is, based on the "end-state comfort effect" (Rosenbaum et al., 1990), given free
748 choice, participants likely would have used the right hand to grasp the object between the thumb and
749 index-finger knuckle, and would have adjusted the grip such that the thumb was lowest when planning
750 to turn left, aligned with the index-finger knuckle when grasping without turning, and highest when
751 planning to turn right. Indeed, had they done so, we would expect even stronger multivariate
752 differences between conditions. Nevertheless, we found multivariate differences even in the case when
753 the low-level grasp posture remained constant (Ariani et al., 2015; Ramon et al., 2015).

754

755 Conclusion

We investigated the neural underpinnings of how hand-object interactions unfold on a moment-to-moment basis. Importantly, we found that the neural underpinnings of grasping and turning actions could best be differentiated in occipital cortex (particularly cIPS and V1) and SPL. These results corroborate the importance of cIPS in processing object and grip orientation and suggest that SPL may play a larger role in action sequences than previously realized. Our results also show how tMVPA can be used to understand how motor actions are represented across different phases of the trial.

**Bibliography**


Ariani, G., Oosterhof, N. N., & Lingnau, A. (2018). Time-resolved decoding of planned delayed and immediate prehension movements. *Cortex*, *99*, 330–345. https://doi.org/10.1016/j.cortex.2017.12.007

Ariani, G., Wurm, M. F., & Lingnau, A. (2015). Decoding internally and externally driven movement plans. *Journal of Neuroscience*, *35*(42), 14160–14171. https://doi.org/10.1523/JNEUROSCI.0596-15.2015

Astafiev, S. v., Stanley, C. M., Shulman, G. L., & Corbetta, M. (2004). Extrastriate body area in human occipital cortex responds to the performance of motor actions. *Nature Neuroscience*, *7*(5), 542–548. https://doi.org/10.1038/nn1241

Badre, D., & Nee, D. E. (2018). Frontal Cortex and the Hierarchical Control of Behavior. *Trends in Cognitive Sciences*, *22*(2), 170–188. https://doi.org/10.1016/j.tics.2017.11.005

Battaglini, P., Muzur, A., Galletti, C., Skrap, M., Brovelli, A., & Fattori, P. (2002). Effects of lesions to area V6A in monkeys. *Experimental Brain Research*, *144*(3), 419–422. https://doi.org/10.1007/s00221-002-1099-4

Beurze, S. M., De Lange, F. P., Toni, I., & Medendorp, W. P. (2007). Integration of target and effector information in the human brain during reach planning. *Journal of Neurophysiology*, *97*(1), 188–199. https://doi.org/10.1152/jn.00456.2006

Beurze, S. M., De Lange, F. P., Toni, I., & Medendorp, W. P. (2009). Spatial and effector processing in the human parietofrontal network for reaches and saccades. *Journal of Neurophysiology*, *101*(6), 3053–3062. https://doi.org/10.1152/jn.91194.2008

Breveglieri, R., Borgomaneri, S., Filippini, M., Tessari, A., Galletti, C., Davare, M., & Fattori, P. (2022). Complementary contribution of the medial and lateral human parietal cortex to grasping: a repetitive TMS study. *Cerebral Cortex*. https://doi.org/10.1093/cercor/bhac404

Caminiti, R., Innocenti, G. M., & Battaglia-Mayer, A. (2015). Organization and evolution of parieto-frontal processing streams in macaque monkeys and humans. *Neuroscience and Biobehavioral Reviews*, *56*, 73–96. https://doi.org/10.1016/j.neubiorev.2015.06.014

Castiello, U. (2005). The neuroscience of grasping. *Nature Reviews. Neuroscience*, *6*(9), 726–736. https://doi.org/10.1038/nrn1744

Cavina-Pratesi, C., Connolly, J. D., Monaco, S., Figley, T. D., Milner, A. D., Schenk, T., & Culham, J. C. (2018). Human neuroimaging reveals the subcomponents of grasping, reaching and pointing actions. *Cortex*, *98*, 128–148. https://doi.org/10.1016/j.cortex.2017.05.018

Cavina-Pratesi, C., Monaco, S., Fattori, P., Galletti, C., McAdam, T. D., Quinlan, D. J., Goodale, M. A., & Culham, J. C. (2010). Functional magnetic resonance imaging reveals the neural substrates of arm transport and grip formation in reach-to-grasp actions in humans. *Journal of Neuroscience*, *30*(31), 10306–10323. https://doi.org/10.1523/JNEUROSCI.2023-10.2010

Comalli, D. M., Keen, R., Abraham, E. S., Foo, V. J., Lee, M. H., & Adolph, K. E. (2016). The development of tool use: Planning for end-state comfort. *Developmental Psychology*, *52*(11), 878–1892. https://doi.org/10.1037/dev0000207

Culham, J. C., Cavina-Pratesi, C., & Singhal, A. (2006). The role of parietal cortex in visuomotor control: What have we learned from neuroimaging? *Neuropsychologia*, *44*(13), 2668–2684. https://doi.org/10.1016/j.neuropsychologia.2005.11.003

Culham, J. C., Danckert, S. L., DeSouza, J. F. X., Gati, J. S., Menon, R. S., & Goodale, M. A. (2003). Visually guided grasping produces fMRI activation in dorsal but not ventral stream brain areas. *Experimental Brain Research*, *153*(2), 180–189. https://doi.org/10.1007/s00221-003-1591-5

Culham, & Kanwisher. (2001). Neuroimaging of cognitive functions in human parietal cortex. *Current Opinion in Neurobiology*.

Errante, A., Ziccarelli, S., Mingolla, G., & Fogassi, L. (2021). Grasping and Manipulation: Neural Bases and Anatomical Circuitry in Humans. *Neuroscience*, *458*, 203–212. https://doi.org/10.1016/j.neuroscience.2021.01.028

Fabbri, S., Stubbs, K. M., Cusack, R., & Culham, J. C. (2016). Disentangling Representations of Object and Grasp Properties in the Human Brain. *The Journal of Neuroscience*, *36*(29), 7648–7662. https://doi.org/10.1523/JNEUROSCI.0313-16.2016

Fischl, B., Sereno, M. I., Tootell, R. B. H., & Dale, A. M. (1999). High-Resolution Intersubject Averaging and aCoordinate System for the Cortical Surface. *Human Brain Mapping*.

Fogassi, L., Ferrari, P. F., Gesierich, B., Rozzi, S., Chersi, F., & Rizzolotti, G. (2005). Parietal lobe: From action organization to intention understanding. *Science*, *308*(5722), 662–667. https://doi.org/10.1126/science.1106138

Frost, M. A., & Goebel, R. (2012). Measuring structural–functional correspondence: Spatial variability of specialised brain regions after macro-anatomical alignment. *NeuroImage*, *59*(2), 1369–1381. https://doi.org/10.1016/j.neuroimage.2011.08.035

Gallivan, J. P., Adam McLean, D., Valyear, K. F., & Culham, J. C. (2013). Decoding the neural mechanisms of human tool use. *ELife*, *2013*(2), 1–29. https://doi.org/10.7554/eLife.00425

Gallivan, J. P., Cant, J. S., Goodale, M. A., & Flanagan, J. R. (2014). Representation of object weight in human ventral visual cortex. *Current Biology*, *24*(16), 1866–1873. https://doi.org/10.1016/j.cub.2014.06.046

Gallivan, J. P., Chapman, C. S., Gale, D. J., Flanagan, J. R., & Culham, J. C. (2019). Selective Modulation of Early Visual Cortical Activity by Movement Intention. *Cerebral Cortex*, 1–17. https://doi.org/10.1093/cercor/bhy345

Gallivan, J. P., & Culham, J. C. (2015). Neural coding within human brain areas involved in actions. In *Current Opinion in Neurobiology* (Vol. 33, pp. 141–149). Elsevier Ltd. https://doi.org/10.1016/j.conb.2015.03.012

Gallivan, J. P., Johnsrude, I. S., & Randall Flanagan, J. (2016). Planning Ahead: Object-Directed Sequential Actions Decoded from Human Frontoparietal and Occipitotemporal Networks. *Cerebral Cortex*, *26*(2), 708–730. https://doi.org/10.1093/cercor/bhu302

Gallivan, J. P., McLean, D. A., Valyear, K. F., Pettypiece, C. E., & Culham, J. C. (2011). Decoding action intentions from preparatory brain activity in human parieto-frontal networks. *Journal of Neuroscience*, *31*(26), 9599–9610.

Gamberini, M., Passarelli, L., Fattori, P., & Galletti, C. (2020). Structural connectivity and functional properties of the macaque superior parietal lobule. *Brain Structure and Function*, *225*(4), 1349–1367. https://doi.org/10.1007/s00429-019-01976-9

Gerbella, M., Rozzi, S., & Rizzolatti, G. (2017). The extended object-grasping network. *Experimental Brain Research*, *235*(10), 2903–2916. https://doi.org/10.1007/s00221-017-5007-3

Goebel, R., Esposito, F., & Formisano, E. (2006). Analysis of Functional Image Analysis Contest (FIAC) data with BrainVoyager QX: From single-subject to cortically aligned group General Linear Model analysis and self-organizing group Independent Component Analysis. *Human Brain Mapping*, *27*(5), 392–401. https://doi.org/10.1002/hbm.20249

Greenfield, A., Jahnsen, H., Downing, P. E., Jiang, Y., Shuman, M., & Kanwisher, N. (1996). A Cortical Area Selective for Visual Processing of the Human Body. In *Trends Pharmacol. Sci* (Vol. 16). https://www.science.org

Grefkes, C., & Fink, G. R. (2005). *The functional organization of the intraparietal sulcus in humans and monkeys*. 3–17.

Greve, D. N., & Fischl, B. (2009). Accurate and Robust Brain Image Alignment using Boundary- based Registration. *Neuroimage*, *48*(1), 63–72. https://doi.org/10.1016/j.neuroimage.2009.06.060.Accurate

Guo, L. L., Nestor, A., Nemrodov, D., Frost, A., & Niemeier, M. (2019). Multivariate analysis of electrophysiological signals reveals the temporal properties of visuomotor computations for precision grips. *Journal of Neuroscience*, *39*(48), 9585–9597. https://doi.org/10.1523/JNEUROSCI.0914-19.2019

Gutteling, T. P., Petridou, N., Dumoulin, S. O., Harvey, B. M., Aarnoutse, E. J., Leon Kenemans, J., & Neggers, S. F. W. (2015). Action preparation shapes processing in early visual cortex. *Journal of Neuroscience*, *35*(16), 6472–6480. https://doi.org/10.1523/JNEUROSCI.1358-14.2015

Haxby, J. V., Gobbini, M. I., Furey, M. L., Ishai, A., Schouten, J. L., & Pietrini, P. (2001). Distributed and overlapping representations of faces and objects in ventral temporal corten. *Science*, *293*(September), 87–96. https://doi.org/10.4324/9780203496190

Hinrichs, H., Scholz, M., Tempelmann, C., Woldorff, M. G., Dale, A. M., & Heinze, H. J. (2000). Deconvolution of event-related fMRI responses in fast-rate experimental designs: Tracking amplitude variations. *Journal of Cognitive Neuroscience*, *12*. https://doi.org/10.1162/089892900564082

Kamitani, Y., & Tong, F. (2005a). Decoding the visual and subjective contents of the human brain. *Nature Neuroscience*.

Kamitani, Y., & Tong, F. (2005b). Decoding the visual and subjective contents of the human brain. *Nature Neuroscience*, *8*(5), 679–685. https://doi.org/10.1038/nn1444

Kontaris, I., Wiggett, A. J., & Downing, P. E. (2009). Dissociation of extrastriate body and biological-motion selective areas by manipulation of visual-motor congruency. *Neuropsychologia*, *47*(14), 3118–3124. https://doi.org/10.1016/j.neuropsychologia.2009.07.012

Kriegeskorte, N. (2008). Representational similarity analysis – connecting the branches of systems neuroscience. *Frontiers in Systems Neuroscience*, *2*(November), 1–28. https://doi.org/10.3389/neuro.06.004.2008

Kriegeskorte, N., & Goebel, R. (2001). An efficient algorithm for topologically correct segmentation of the cortical sheet in anatomical MR volumes. *NeuroImage*, *14*(2), 329–346. https://doi.org/10.1006/nimg.2001.0831

Kriegeskorte, N., & Kievit, R. A. (2013). Representational geometry: Integrating cognition, computation, and the brain. *Trends in Cognitive Sciences*, *17*(8), 401–412. https://doi.org/10.1016/j.tics.2013.06.007

Monaco, S., Cavina-Pratesi, C., Sedda, A., Fattori, P., Galletti, C., & Culhaml, J. C. (2011). Functional magnetic resonance adaptation reveals the involvement of the dorsomedial stream in hand orientation for grasping. *Journal of Neurophysiology*, *106*(5), 2248–2263. https://doi.org/10.1152/jn.01069.2010

Monaco, S., Malfatti, G., Culham, J. C., Cattaneo, L., & Turella, L. (2020). Decoding motor imagery and action planning in the early visual cortex: Overlapping but distinct neural mechanisms. *NeuroImage*, *218*(May), 116981. https://doi.org/10.1016/j.neuroimage.2020.116981

Mylius, V., Ayache, S. S., Ahdab, R., Farhat, W. H., Zouari, H. G., Belke, M., Brugières, P., Wehrmann, E., Krakow, K., Timmesfeld, N., Schmidt, S., Oertel, W. H., Knake, S., & Lefaucheur, J. P. (2013). Definition of DLPFC and M1 according to anatomical landmarks for navigated brain stimulation: inter-rater reliability, accuracy, and influence of gender and age. *NeuroImage*, *78*, 224–232. https://doi.org/10.1016/j.neuroimage.2013.03.061

Passarelli, L., Gamberini, M., & Fattori, P. (2021). The superior parietal lobule of primates: A sensory-motor hub for interaction with the environment. In *Journal of Integrative Neuroscience* (Vol. 20, Issue 1, pp. 157–171). IMR Press Limited. https://doi.org/10.31083/J.JIN.2021.01.334

Pertzov, Y., Avidan, G., & Zohary, E. (2011). Multiple reference frames for saccadic planning in the human parietal cortex. *Journal of Neuroscience*, *31*(3), 1059–1068. https://doi.org/10.1523/JNEUROSCI.3721-10.2011

Picard, N., & Strick, P. L. (2001). Imaging the premotor areas. *Current Opinion in Neurobiology*, *11*(6), 663–672. https://doi.org/10.1016/S0959-4388(01)00266-5

Pilacinski, A., Wallscheid, M., & Lindner, A. (2018). Human posterior parietal and dorsal premotor cortex encode the visual properties of an upcoming action. *PLoS ONE*, *13*(10), 1–20. https://doi.org/10.1371/journal.pone.0198051

Pitzalis, S., Fattori, P., & Galletti, C. (2015). The human cortical areas V6 and V6A. In *Visual Neuroscience* (Vol. 32). Cambridge University Press. https://doi.org/10.1017/S0952523815000048

Ramon, M., Vizioli, L., Liu-Shuang, J., & Rossion, B. (2015). Neural microgenesis of personally familiar face recognition. *Proceedings of the National Academy of Sciences of the United States of America*, *112*(35), E4835–E4844. https://doi.org/10.1073/pnas.1414929112

Rice, N. J., Valyear, K. F., Goodale, M. A., Milner, A. D., & Culham, J. C. (2007). Orientation sensitivity to graspable objects: An fMRI adaptation study. *NeuroImage*, *36*(SUPPL. 2). https://doi.org/10.1016/j.neuroimage.2007.03.032

Richter, M., Amunts, K., Mohlberg, H., Bludau, S., Eickhoff, S. B., Zilles, K., & Caspers, S. (2019). Cytoarchitectonic segregation of human posterior intraparietal and adjacent parieto-occipital sulcus and its relation to visuomotor and cognitive functions. *Cerebral Cortex*, *29*(3), 1305–1327. https://doi.org/10.1093/cercor/bhy245

Rizzolatti, G., & Matelli, M. (2003). Two different streams form the dorsal visual system: Anatomy and functions. *Experimental Brain Research*, *153*(2), 146–157. https://doi.org/10.1007/s00221-003-1588-0

Rosenbaum, D. A., Marchak, F., Barnes, H. J., Vaughan, J., Slotta, J. D., & Jorgensen, M. J. (1990). Constraints for Action Selection: Overhand Versus Underhand Grips. *Attention and Performance XIII: Motor Representation and Control*, *August 2014*, 321–342. https://doi.org/10.4324/9780203772010-10

Rosenke, M., van Hoof, R., van den Hurk, J., Grill-Spector, K., & Goebel, R. (2021). A Probabilistic Functional Atlas of Human Occipito-Temporal Visual Cortex. *Cerebral Cortex*, *31*(1), 603–619. https://doi.org/10.1093/cercor/bhaa246

Scheperjans, F., Eickhoff, S. B., Hömke, L., Mohlberg, H., Hermann, K., Amunts, K., & Zilles, K. (2008). Probabilistic maps, morphometry, and variability of cytoarchitectonic areas in the human superior parietal cortex. *Cerebral Cortex*, *18*(9), 2141–2157. https://doi.org/10.1093/cercor/bhm241

Scheperjans, F., Hermann, K., Eickhoff, S. B., Amunts, K., Schleicher, A., & Zilles, K. (2008). Observer-independent cytoarchitectonic mapping of the human superior parietal cortex. *Cerebral Cortex*, *18*(4), 846–867. https://doi.org/10.1093/cercor/bhm116

Shikata, E., Hamzei, F., Glauche, V., Knab, R., Dettmers, C., Weiller, C., Bu¨chel, C., & Bu¨chel, B. (2001). *Surface Orientation Discrimination Activates Caudal and Anterior Intraparietal Sulcus in Humans: An Event-Related fMRI Study*. www.jn.physiology.org

Singhal, A., Monaco, S., Kaufman, L. D., & Culham, J. C. (2013). Human fMRI Reveals That Delayed Action Re-Recruits Visual Perception. *PLoS ONE*, *8*(9). https://doi.org/10.1371/journal.pone.0073629

Tomassini, V., Jbabdi, S., Klein, J. C., Behrens, T. E. J., Pozzilli, C., Matthews, P. M., Rushworth, M. F. S., & Johansen-Berg, H. (2007). Diffusion-weighted imaging tractography-based parcellation of the human lateral premotor cortex identifies dorsal and ventral subregions with anatomical and functional specializations. *Journal of Neuroscience*, *27*(38), 10259–10269. https://doi.org/10.1523/JNEUROSCI.2144-07.2007

Valyear, K. F., Culham, J. C., Sharif, N., Westwood, D., & Goodale, M. A. (2006). A double dissociation between sensitivity to changes in object identity and object orientation in the ventral and dorsal visual streams: A human fMRI study. *Neuropsychologia*, *44*(2), 218–228. https://doi.org/10.1016/j.neuropsychologia.2005.05.004

van den Heiligenberg, F. M. Z., Orlov, T., Macdonald, S. N., Duff, E. P., Henderson Slater, D., Beckmann, C., Johansen-Berg, H., Culham, J. C., & Makin, T. R. (2018). Artificial limb representation in amputees. *Brain*, *March*, 1–12. https://doi.org/10.1093/brain/awy054

Vizioli, L., Bratch, A., Lao, J., Ugurbil, K., Muckli, L., & Yacoub, E. (2018). Temporal multivariate pattern analysis (tMVPA): A single trial approach exploring the temporal dynamics of the BOLD signal. *Journal of Neuroscience Methods*, *308*(June 2018), 74–87. https://doi.org/10.1016/j.jneumeth.2018.06.029

Wandell, B. A., Dumoulin, S. O., & Brewer, A. A. (2007). Visual field maps in human cortex. In *Neuron* (Vol. 56, Issue 2, pp. 366–383). https://doi.org/10.1016/j.neuron.2007.10.012

Wood, D. K., Chouinard, P. A., Major, A. J., & Goodale, M. A. (2017). Sensitivity to biomechanical limitations during postural decision-making depends on the integrity of posterior superior parietal cortex. *Cortex*, *97*, 202–220. https://doi.org/10.1016/j.cortex.2016.07.005

Yousry, T. A., Schmid, U. D., Alkadhi, H., Schmidt, D., Peraud, A., Buettner, A., & Winkler, P. (1997). Localization of the motor hand area to a knob on the precentral gyrus A new landmark. *Brain*, 141–157.

Zimmermann, M., Mars, R. B., de Lange, F. P., Toni, I., & Verhagen, L. (2018). Is the extrastriate body area part of the dorsal visuomotor stream? *Brain Structure and Function*, *223*(1), 31–46. https://doi.org/10.1007/s00429-017-1469-0

Zimmermann, M., Verhagen, L., de Lange, F. P., & Toni, I. (2016). The extrastriate body area computes desired goal states during action planning. *ENeuro*, *3*(2), 1918–1921. https://doi.org/10.1523/ENEURO.0020-16.2016

**Number of Voxels Per Region of Interest**

| Region of Interest | Number of Functional Voxels |
|---|---|
| M1 | 98 ± 7 |
| S1 | 123 ± 11 |
| PMv | 107 ± 8 |
| PMd | 217 ± 9 |
| aSPOC | 178 ± 14 |
| pSPOC | 138 ± 7 |
| aIPS | 268 ± 17 |
| cIPS | 172 ± 10 |
| Pre-SMA | 108 ± 7 |
| SMA | 132 ± 10 |
| DLPFC | 129 ± 9 |
| V1d | 152 ± 13 |
| Area-5L | 167 ± 10 |
| Area-7A | 194 ± 12 |
| Area-7P | 150 ± 9 |
| Area-7PC | 198 ± 13 |
| EBA | 1163 ± 23 |

**Table 1.** The average number of functional (1-mm iso-)voxels per Region of Interest. Values shown are mean ± SEM.

## Figure legends

**Figure 1.** Experimental set-up and design. **1A.** Picture of participant set-up in the fMRI scanner shown from side view. **1B.** Close up of participant using the instructed grip to grasp the experimental stimulus, i.e., rotatable dial with a handle. **1C.** Experimental conditions in a two (start orientation: left or right) by two (action: grasp or turn) design. **2D.** Timing of each event-related trial. Trials began with the stimulus being illuminated (TR 0-3) indicating the start of the preparation phase. At TR 3 participants received task instructions indicating the start of the planning phase (TR 3-9). At TR 9 participants received the "go" cue indicating onset of action execution (TR 9-10). After 2 s (1 TR) the light was turned off and the intertrial interval was initiated (TR 10-16).

**Figure 2.** Brain areas selected for multivariate analysis based on a univariate contrast. Cortical areas that exhibited larger responses during the experimental trials [(presentation + plan + execute) > baseline] are shown in yellow to red activation. Results calculated across all participants (RFX GLM) are displayed on the dynamic group average surface across participants. The selected ROIs were selected in BrainVoyager software, which uses a hexagonal selection area, and then transformed to individual volumetric MNI space. Each ROI is linked to the group average of corresponding % signal change of BOLD activity (Y-axis) over time (X-axis; each X-ticks represents one TR of 2 s, based on a deconvolution analysis) for each of the four conditions. Vertical dashed lines on the graphs indicate start of the planning phase (TR 3) and the execution phase (TR 9). Sulcal landmarks are denoted by white lines (stylized according to the corresponding legend). ROI acronyms are spelled out in the methods. tMVPA results are indicated using different types of circles (e.g., dashed vs. solid). RSA results are shown by color-coding the tMVPA circles using a Venn diagram. Note that the RSA and tMVPA results are discussed in the results section as well as in Figure 5 and Figure 6.

**Figure 3.** Overview of the steps to perform temporal multivoxel pattern analysis (see methods for full explanation). The figure represents the steps taken for each participant separately. Within each condition single trial representational distance matrices (RDMs) are calculated for each timepoint of each trial pairing (**3A** shows example for grasping trials and **3B** for turning trials). **3C:** Grey cubes represent voxels of the same ROI during different timepoints for two sample trials to exemplify how cells for each RDM are calculated. After calculating single trial RDMs, a condition average is calculated (middle column; **3D** and **3E** for grasping and turning respectively) which are then subtracted from each other (last column; **3F**; red and blue matrix). Not shown on picture (for results see Figure 4 and 5): the subtraction matrices are then used for bootstrapping to determine whether the group average differs significantly from zero and to investigate whether one condition is more similar than the other for each given timepoint

**Figure 4.** Models used for representational similarity analysis (RSA). The first row shows the models for start orientation (**4A**), end orientation (**4B**) and turn versus grasp (**4C**). The second row shows example data for one single timepoint for two regions of interest (**4D**: V1d); **4E**: Area-7A) of one participant.

**Figure 5. Left:** Hierarchical clustering of all the ROIs based on the averaged representational dissimilarity matrices (RDMs) of the **Grasp** and **Turn** condition. We refer the reader to the legend of Figure 3 for the full explanation of the heatmaps. Note that **T-G** represents 'Turn minus Grasp' and represents the final tMVPA result showing statistically significant similarities (small red boxes = Turn > Grasp; small green boxes = Grasp > Turn).

1052 **Figure 6.** Selection of ROIs that showed prominent differences for the tMVPA analysis. Some
1053 data are reproduced from subsets of Figures 2 (Column 1) and 5 (Columns 2-4, at higher resolution) to
1054 facilitate inspection and comparisons across analysis methods for key regions. **Column 1** shows the
1055 group average deconvolution time courses for the four conditions. The X-axis represents time (in 2 s
1056 TRs) and the Y-axis represents % signal change in the BOLD signal. Vertical dashed lines represent onset
1057 of the planning phase (TR 3) (after the initial presentation phase) and the execution phase (TR 9)
1058 following the planning phase. **Columns 2 and 3** show the group average condition representational
1059 dissimilarity matrices for the grasp (column 2) and turn condition (column 3). Each cell/square of the
1060 matrix represents the dissimilarity between trials of the same condition between two timepoints.
1061 Dashed horizontal and vertical lines represent the same timepoints as those in Column 1, i.e., the first
1062 dashed horizontal/vertical line represents the start of the planning phase (TR 3) and the second dashed
1063 vertical/horizontal line represents the start of the execution phase (TR 9). **Column 4**. tMVPA results.
1064 Dashed lines have the same representation as explained for columns 1-3. Red squares indicate
1065 dissimilarity metrics between timepoints where turning trials are significantly more similar (less
1066 dissimilar) than grasping trials. Green squares represent the opposite (grasping more similar than
1067 turning). **Column 5.** Representational similarity analysis using three models, as explained in the color
1068 legend, for each timepoint of the experimental trials. Solid lines represent the correlation between the
1069 data and the model over time. The shaded grey area represents the noise ceiling with the lower and
1070 upper edges representing the lower and upper bounds. Dashed vertical lines have the same
1071 representation as explained for the previous columns. Colored asterisks indicate time points with
1072 statistically significant correlations for the respective model.

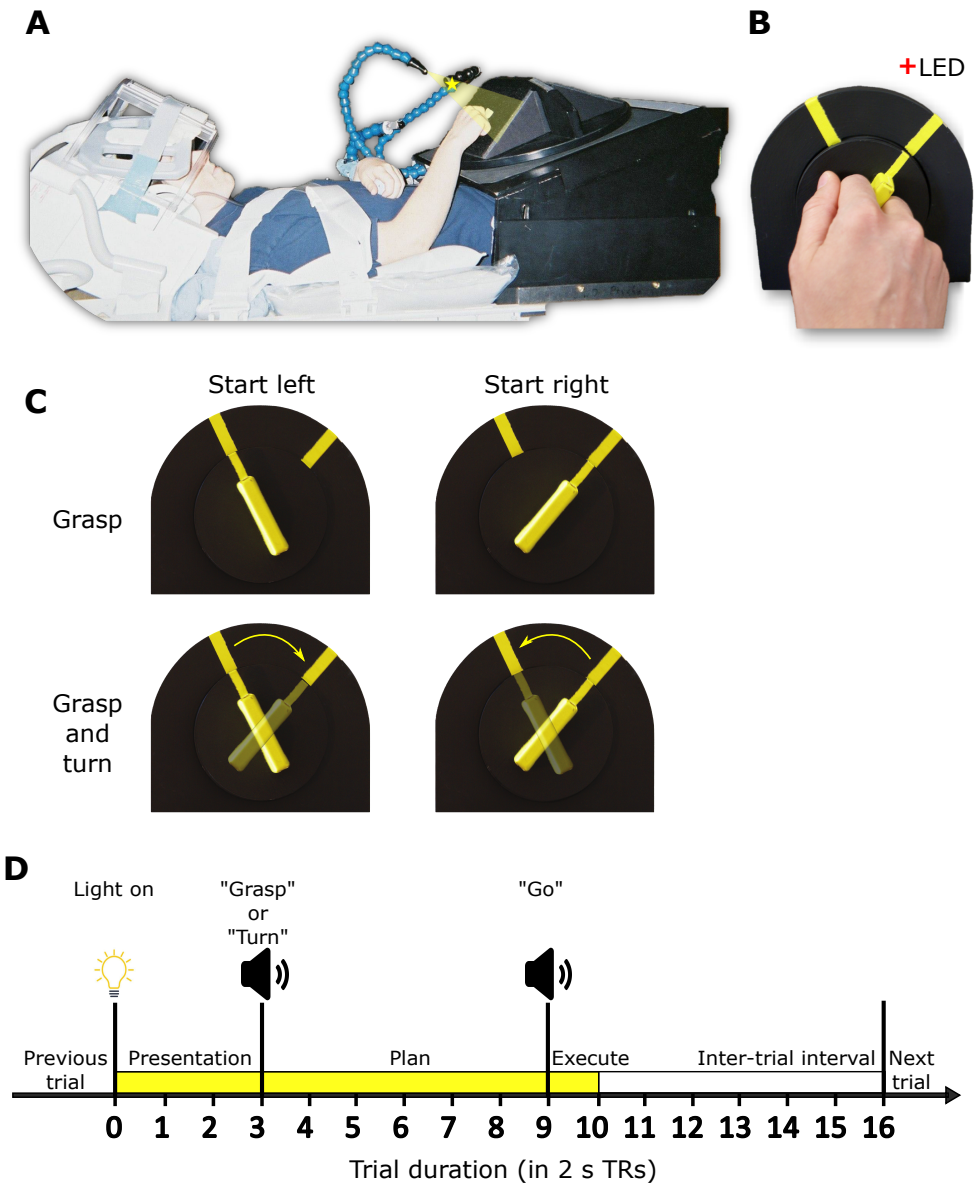
A
B
+LED
C
Start left
Start right
Grasp
Grasp and turn
D
Light on
"Grasp" or "Turn"
"Go"
Previous trial
Presentation
Plan
Execute
Inter-trial interval
Next trial
0 1 2 3 4 5 6 7 8 9 10 11 12 13 14 15 16
Trial duration (in 2 s TRs)

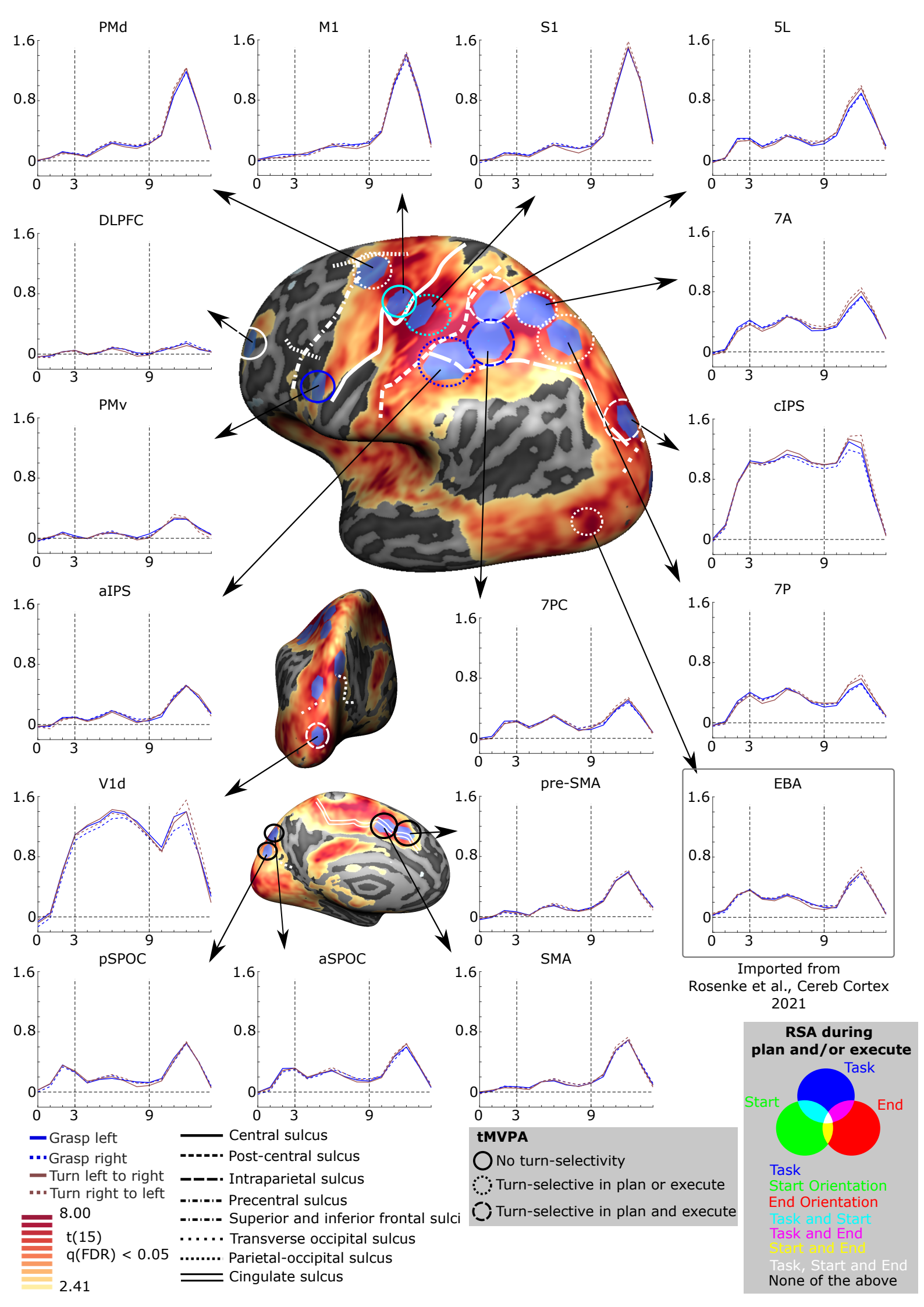
PMd
M1
S1
5L
DLPFC
7A
PMv
cIPS
aIPS
7PC
7P
V1d
pre-SMA
EBA
pSPOC
aSPOC
SMA
1.6
0.8
0
0
3
9
Imported from
Rosenke et al., Cereb Cortex
2021
Grasp left
Grasp right
Turn left to right
Turn right to left
8.00
t(15)
q(FDR) < 0.05
2.41
Central sulcus
Post-central sulcus
Intraparietal sulcus
Precentral sulcus
Superior and inferior frontal sulci
Transverse occipital sulcus
Parietal-occipital sulcus
Cingulate sulcus
tMVPA
No turn-selectivity
Turn-selective in plan or execute
Turn-selective in plan and execute
RSA during
plan and/or execute
Task
Start
End
Task
Start Orientation
End Orientation
Task and Start
Task and End
Start and End
Task, Start and End
None of the above

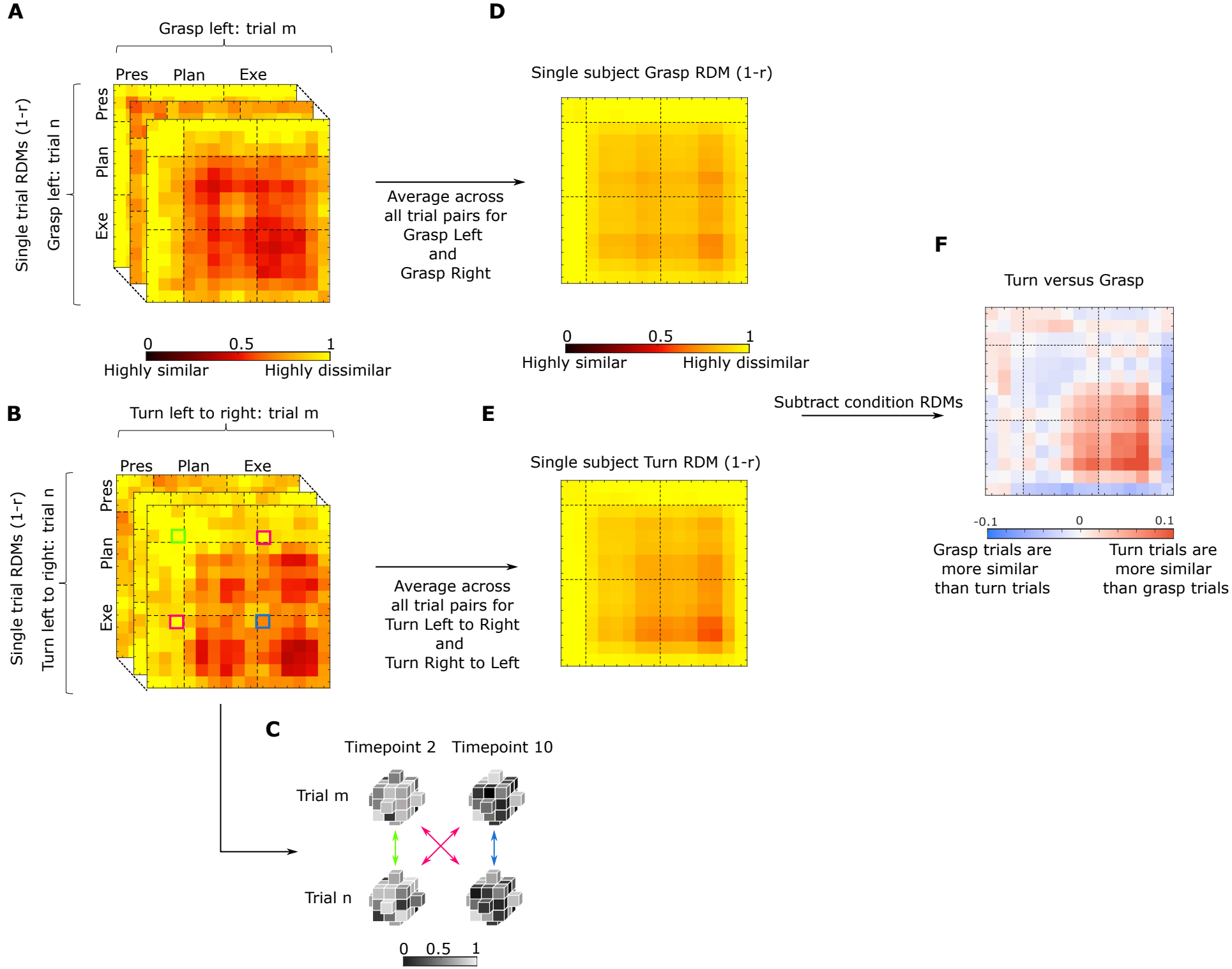
A
Grasp left: trial m
Pres
Plan
Exe
Single trial RDMs (1-r)
Grasp left: trial n
0
0.5
1
Highly similar
Highly dissimilar
D
Single subject Grasp RDM (1-r)
Average across
all trial pairs for
Grasp Left
and
Grasp Right
0
0.5
1
Highly similar
Highly dissimilar
F
Turn versus Grasp
Subtract condition RDMs
-0.1
0
0.1
Grasp trials are
more similar
than turn trials
Turn trials are
more similar
than grasp trials
B
Turn left to right: trial m
Pres
Plan
Exe
Single trial RDMs (1-r)
Turn left to right: trial n
E
Single subject Turn RDM (1-r)
Average across
all trial pairs for
Turn Left to Right
and
Turn Right to Left
C
Timepoint 2
Timepoint 10
Trial m
Trial n
0
0.5
1

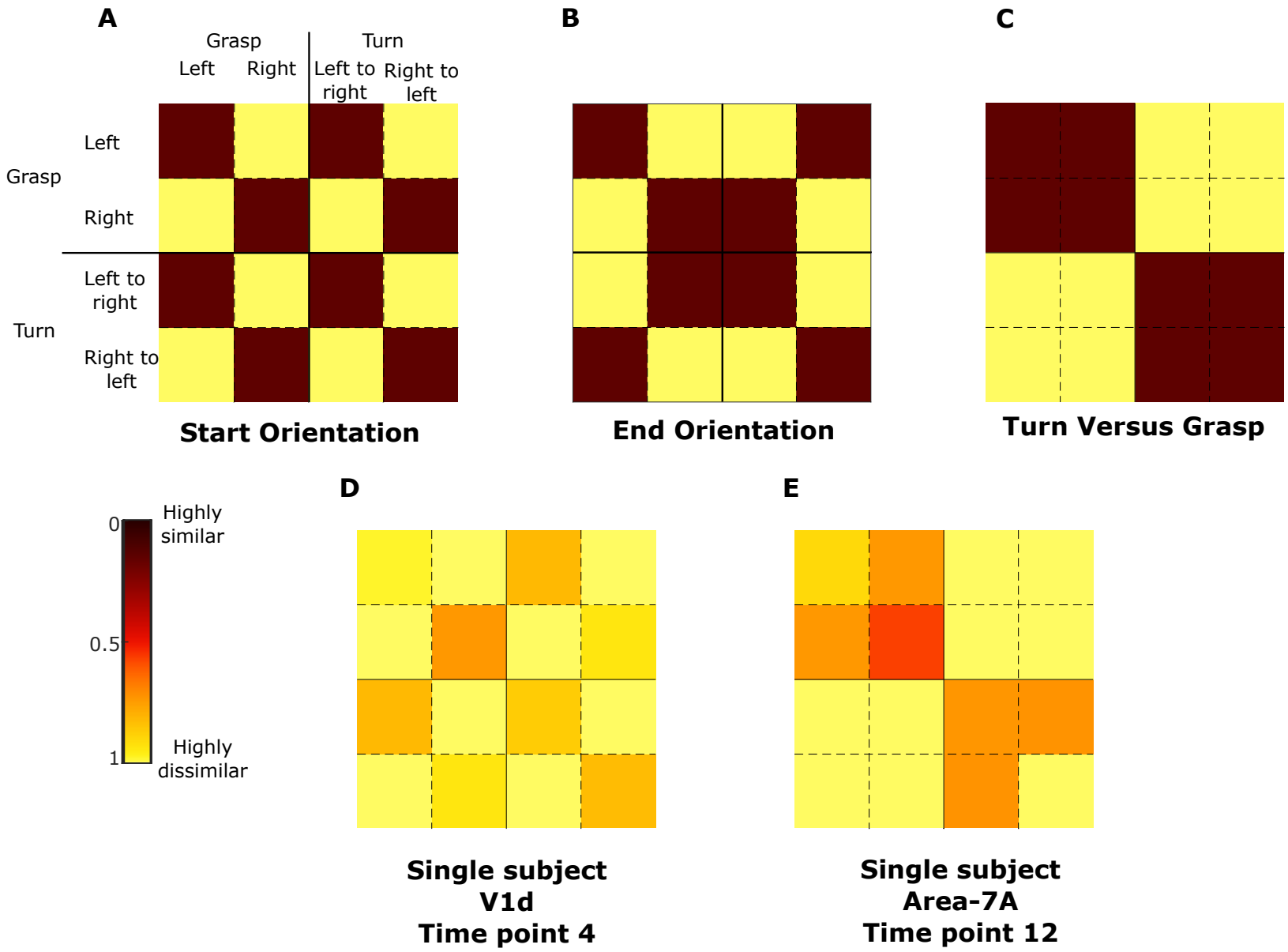
A
Grasp
Turn
Left
Right
Left to right
Right to left
Grasp
Left
Right
Turn
Left to right
Right to left
Start Orientation
B
End Orientation
C
Turn Versus Grasp
0
Highly similar
0.5
1
Highly dissimilar
D
Single subject
V1d
Time point 4
E
Single subject
Area-7A
Time point 12

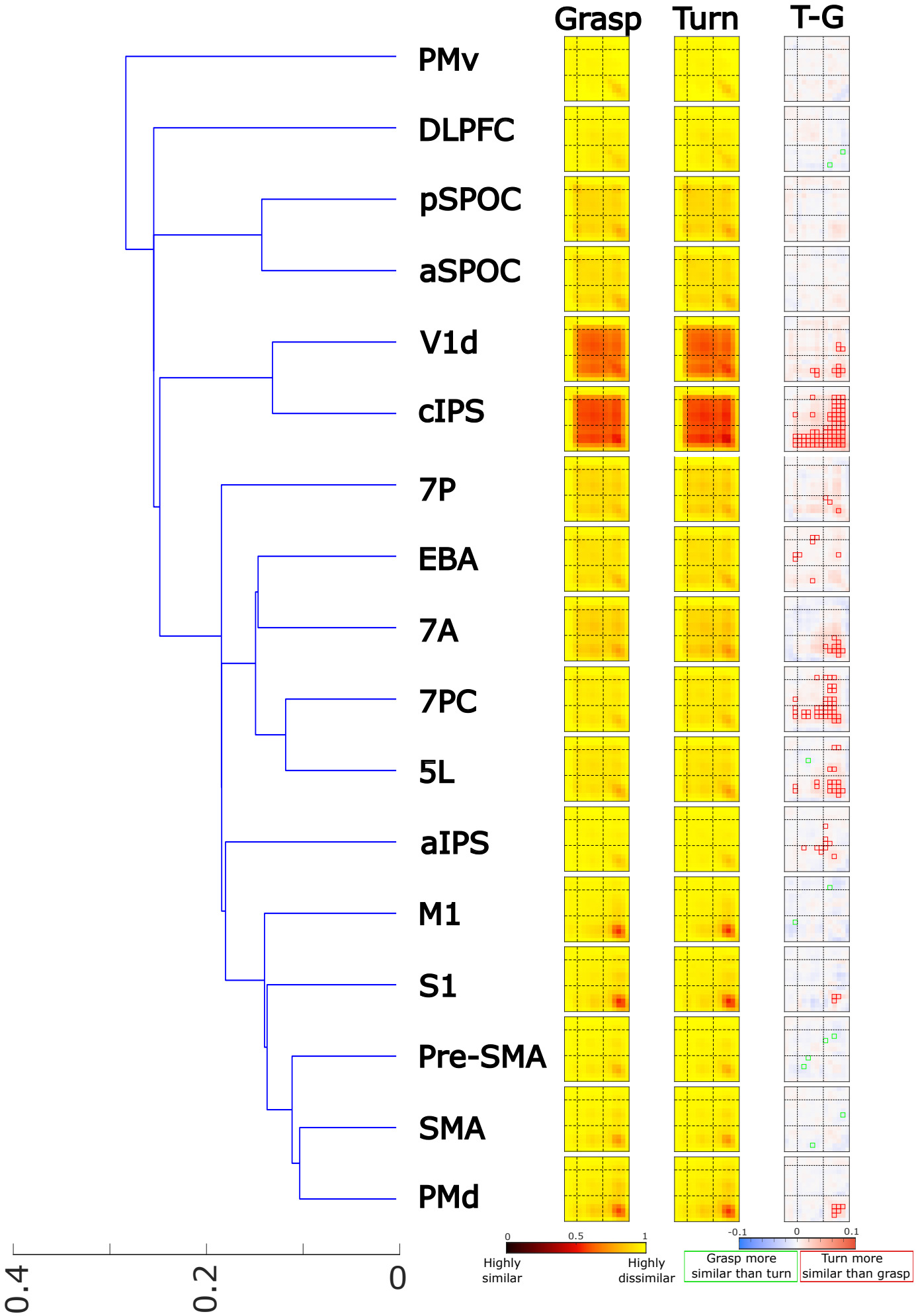
Grasp
Turn
T-G
PMv
DLPFC
pSPOC
aSPOC
V1d
cIPS
7P
EBA
7A
7PC
5L
aIPS
M1
S1
Pre-SMA
SMA
PMd
0.4
0.2
0
0
0.5
1
Highly similar
Highly dissimilar
-0.1
0
0.1
Grasp more similar than turn
Turn more similar than grasp

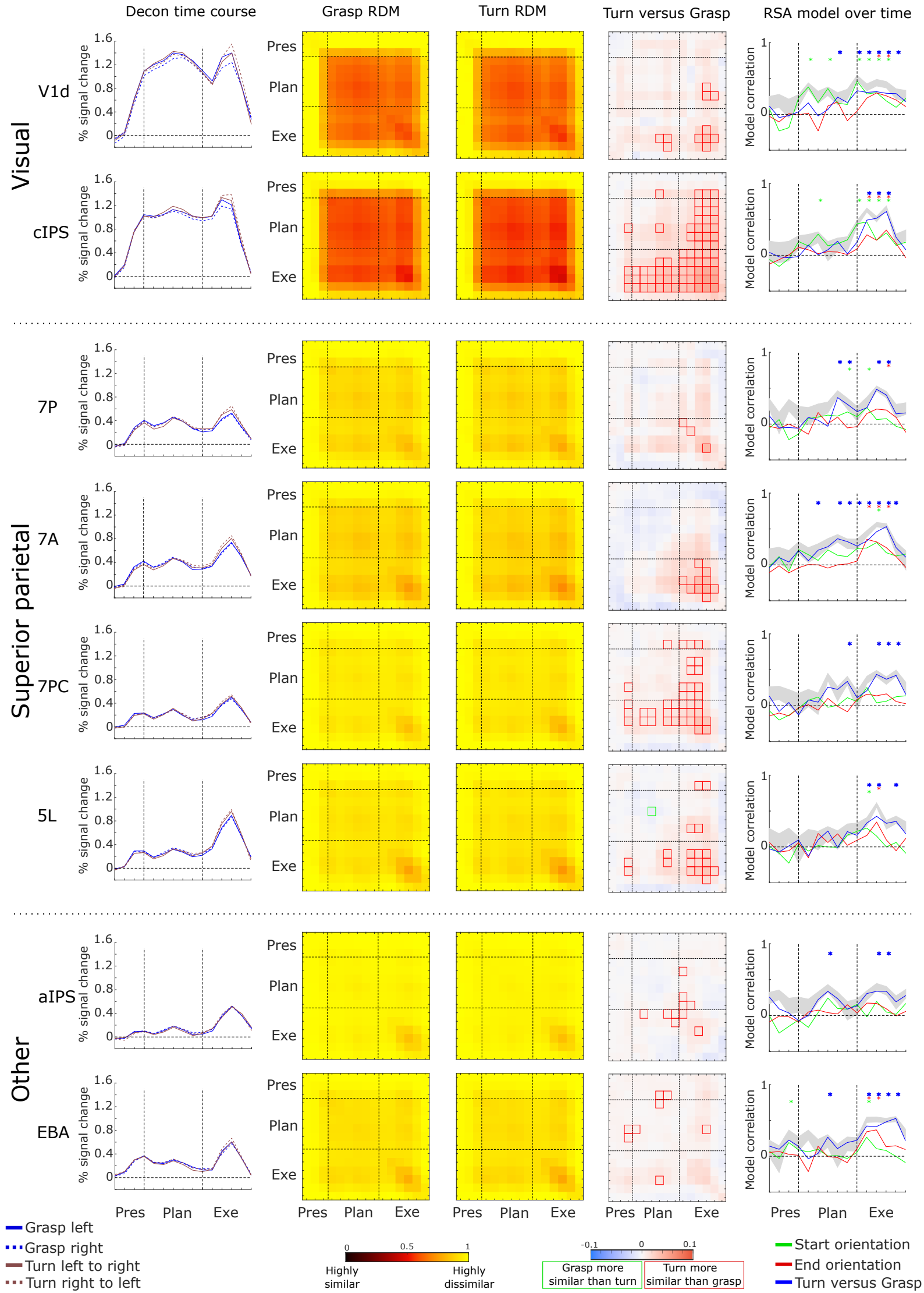
Decon time course
Grasp RDM
Turn RDM
Turn versus Grasp
RSA model over time
Visual
V1d
cIPS
Superior parietal
7P
7A
7PC
5L
Other
aIPS
EBA
% signal change
Model correlation
Pres
Plan
Exe
Grasp left
Grasp right
Turn left to right
Turn right to left
Highly similar
Highly dissimilar
Grasp more similar than turn
Turn more similar than grasp
Start orientation
End orientation
Turn versus Grasp